Research Square

Preprints are preliminary reports that have not undergone peer review.
They should not be considered conclusive, used to inform clinical practice,
or referenced by the media as validated information.

Mechanical coordination of counter-gradient growth maintains organ curvature in the apical hook

Stéphanie Robert

stephanie.robert@slu.se

Umeå Plant Science Centre, Department of Forest Genetics and Plant Physiology, Swedish University of Agricultural Sciences https://orcid.org/0000-0002-0013-3239

Sara Raggi

Umeå Plant Science Centre, Department of Forest Genetics and Plant Physiology, Swedish University of Agricultural Sciences

Hemamshu Ratnakaram

Umeå Plant Science Centre, Department of Forest Genetics and Plant Physiology, Swedish University of Agricultural Sciences https://orcid.org/0009-0004-9983-4562

Adrien Heymans

Life Institute, Université catholique de Louvain

Loitongbam Devi

Umeå Plant Science Centre, Department of Forest Genetics and Plant Physiology, Swedish University of Agricultural Sciences

Özer Erguvan

Umeå Plant Science Centre, Department of Forest Genetics and Plant Physiology, Swedish University of Agricultural Sciences

Siamsa Doyle

Umeå Plant Science Centre https://orcid.org/0000-0003-4889-3496

François Jobert

Asal Atakhani

Umeå Plant Science Centre, Department of Plant Physiology, Umeå University

Sijia Liu

College of Horticulture, Shenyang Agricultural University, Shenyang

Manuel Petit

Laboratoire Reproduction et Développement des Plantes, Univ Lyon, ENS de Lyon, UCB Lyon, CNRS, INRAE, INRIA

Jürgen Kleine-Vehn

University of Freiburg/Institute of Biology II

Krzysztof Wabnik
Centro de Biotecnologıa y Genomica de Plantas (Universidad Politecnica de Madrid - Instituto Nacional de Investigacion y Tecnologıa Agraria y Alimentaria) https://orcid.org/0000-0001-7263-0560
Stéphane Verger
Umeå Plant Science Centre, Department of Plant Physiology, Umeå University

---

Article

Keywords:

Posted Date: June 3rd, 2026

DOI: https://doi.org/10.21203/rs.3.rs-9901835/v1

License: This work is licensed under a Creative Commons Attribution 4.0 International License.
Read Full License

Additional Declarations: There is **NO** Competing Interest.

Mechanical coordination of counter-gradient growth maintains organ curvature in the apical hook

Sara Raggi[1§], Hemamshu Ratnakaram[1§], Adrien Heymans[1,2,8], Loitongbam Lorinda Devi[1], Özer Erguvan[1], Siamsa M. Doyle[1], François Jobert[1,9], Asal Atakhani[2], Sijia Liu[1,10], Manuel Petit[3], Jürgen Kleine-Vehn[4,5], Krzysztof Wabnik[6,7], Stéphane Verger[1,2] and Stéphanie Robert[1*]

ORCIDs:
Sara Raggi: 0000-0002-7925-5772
Hemamshu Ratnakaram: 0009-0004-9983-4562
Adrien Heymans: 0000-0003-3685-2240
Loitongbam Lorinda Devi: 0000-0001-5401-2304
Özer Erguvan: 0000-0002-6873-9341
Siamsa M. Doyle: 0000-0003-4889-3496
François Jobert: 0000-0002-1939-2214
Asal Atakhani: 0000-0002-3944-6996
Sijia Liu: 0000-0002-3203-880X
Manuel Petit: 0000-0002-3211-0066
Jürgen Kleine-Vehn: 0000-0002-4354-3756
Krzysztof Wabnik: 0000-0001-7263-0560
Stéphane Verger: 0000-0003-3643-3978
Stéphanie Robert: 0000-0002-0013-3239

[1]Umeå Plant Science Centre, Department of Forest Genetics and Plant Physiology, Swedish University of Agricultural Sciences, SE-901 83 Umeå, Sweden
[2]Umeå Plant Science Centre, Department of Plant Physiology, Umeå University, SE-90183 Umeå, Sweden
[3]Laboratoire Reproduction et Développement des Plantes, Univ Lyon, ENS de Lyon, UCB Lyon, CNRS, INRAE, INRIA, F-69342 Lyon, France
[4]Institute of Biology II, Division of Molecular Plant Physiology (MoPP), University of Freiburg, 79104 Freiburg, Germany
[5]Center for Integrative Biological Signaling Studies (CIBSS), University of Freiburg, 79104 Freiburg, Germany
[6]Centro De Biotecnología Y Genómica De Plantas, Universidad Politécnica De Madrid (Upm), Instituto Nacional De Investigación Y Tecnología Agraria Y Alimentaria (Inia, Csic), Campus De Montegancedo, Pozuelo De Alarcón, 28223, Madrid, Spain
[7]Departamento de Biotecnología-Biología Vegetal, Escuela Técnica Superior de Ingeniería Agronómica, Alimentaria y de Biosistemas, Universidad Politécnica de Madrid (UPM), Madrid, 28040, Spain
[8]Present address: Earth and Life Institute, Université catholique de Louvain, UCLouvain, Belgium
[9]Present address: Université de Picardie Jules Verne (UPJV), Amiens, France
[10]Present address: College of Horticulture, Shenyang Agricultural University, Shenyang, 110866, China
§ These authors contributed equally to this work.
*Corresponding author (Stephanie.Robert@slu.se).

Abstract

How growing tissues convert mechanical forces to stable organ shapes remains a central question in morphogenesis. Curved organ shapes in plants arise from differential growth, yet how curvature is actively maintained while organs continuously grow remains poorly understood. In etiolated seedlings, the apical hook provides a tractable model to dissect this process. Using quantitative imaging, computational modelling, and genetics, we show that antagonistic growth gradients at apical and basal regions are required to sustain hook curvature during growth. Cuticle integrity is a key regulator of these opposing growth programs, linking tissue mechanics to spatial control of cellular elongation. Furthermore, reactive oxygen species (ROS) act downstream of mechanical cues to coordinate growth responses across the tissue. Together, these findings identify a mechanochemical feedback mechanism that maintains organ curvature during continuous growth by stabilizing opposing growth domains. This work provides a mechanistic framework for how developing tissues preserve shape under ongoing growth.

Introduction

Organ morphogenesis emerges from the spatiotemporal regulation of differential growth, whereby local domains of tissue undergo distinct rates and orientations of cell expansion to produce organ-specific geometries. Plant cell expansion is a mechanically constrained process governed by the interplay between intracellular turgor pressure and the viscoelastic properties of the cell wall, a polysaccharide network located outside the plasma membrane. The anisotropic mechanical properties of the wall, largely dictated by the spatial organization of cellulose microfibrils, the cross-linking of hemicelluloses, and the biochemical status of pectins, impose directional constraints that define the axis of cell elongation and ultimately organ shape[1,2]. Plant cells can be conceptualized as pressurized cylinders in which turgor-generated tensile stress exerts forces on the surrounding wall matrix. Irreversible expansion occurs only when the wall undergoes controlled yielding through enzymatic remodeling, mediated by wall-loosening agents such as expansins, xyloglucan endotransglycosylases, and other polysaccharide-modifying enzymes, concomitant with the incorporation of newly synthesized wall polymers to preserve structural integrity[3–5]. Growth heterogeneity, such as when the cell elongates in one direction, is mediated by anisotropic cell wall loosening, cytoskeletal dynamics, and differential deposition of cell wall polymers, processes that are themselves tightly modulated by gradients of hormones such as auxin [6,7]. At the tissue scale, the coordinated integration of these local growth patterns generates emergent mechanical stresses that create feedback to influence growth axes and anisotropy[8].

In the natural environment, seedlings germinate in darkness surrounded by soil, under mechanically abrasive conditions that can hinder proper emergence. To cope with these challenges, dicotyledonous plants have evolved a transient inverted-U-shaped structure at the tip of the hypocotyl called the apical hook, which plays a vital protective role, shielding the shoot apical meristem and cotyledons during soil emergence. Apical hook development unfolds in three distinct phases: formation, maintenance, and opening[9]. Following germination, the hook is established through differential growth across the hypocotyl, with cells on one side elongating faster than those on the opposite side, driving hypocotyl arching[9,10]. During the maintenance phase, differential growth continues at a stable rate, sustaining hook curvature. Hook straightening later occurs during the opening phase, when cells on the inner side elongate more rapidly than those on the outer side. During apical hook development, gradients of cell expansion translate directly into visually perceptible organ bending. This makes the apical hook

a valuable model for dissecting the complex interactions among signaling networks, hormone gradients, biomechanical cues, cell growth parameters, and organ morphogenesis[11–16]. Mechanical feedback, mediated through wall stress and strain, integrates with gradients of hormones such as auxin, gibberellin, and ethylene to coordinate asymmetric growth, ensuring robust formation and maintenance of the hook structure[12,15,17].

The outer cell walls of epidermal cells at the surface of plant above-ground organs, including the apical hook, and transiently, the root meristem, are covered by a waxy, lipid-rich extracellular layer called the cuticle[18,19]. This ancient structure emerged during the transition of plants to land, primarily to prevent dehydration and provide mechanical rigidity to early land plant structures[20]. During evolution, the cuticle has since acquired additional roles beyond water retention, including protection against biotic and abiotic stresses, as well as acting as a core determinant of plant development[18,21].

Reactive oxygen species (ROS) are continuously produced in plants as by-products of metabolism but are also generated in a regulated manner by enzymatic systems such as NADPH oxidases in response to developmental and environmental cues[22–25]. In addition to their signaling functions[26], ROS participate in cell wall remodeling and cuticle formation by promoting oxidative cross-linking of wall polymers and influencing cutin and wax assembly. Notably, cuticle-defective mutants often display altered ROS accumulation and signaling, highlighting a tight functional interplay between redox homeostasis, cell wall architecture, and cuticle integrity[27,28].

Here, we show using quantitative imaging, genetic perturbations, and computational modeling that opposing growth gradients at the apical and basal halves of the apical hook are required to maintain curvature, with cuticle integrity being essential for establishing these gradients. Our data reveal that mechanical cues from the cuticle, together with ROS, coordinate the morphogenetic program, and disruptions in either system destabilize hook curvature. These results highlight how mechanical and biochemical signals integrate to control organ-scale morphogenesis.

Results

Coordinated antagonistic growth dynamics maintain apical hook curvature

While the cellular mechanisms underlying hook formation and opening are well characterized[13], the processes sustaining curvature during the maintenance phase remain poorly understood. Previous studies have suggested that antagonistic growth gradients on opposite sides of the apical–basal midline preserve hook shape [9,13,29–31]. To develop a deeper morphogenetic understanding of these gradients, we generated a high-resolution spatial map of cell elongation across the apical hook. We performed time-lapse confocal imaging of *Arabidopsis thaliana* seedlings expressing the plasma membrane marker *p35S::PIP2A-GFP* over 8 hours. Seedlings with fully formed hooks were chosen for imaging ~24 to 32 hours after germination (T0) and subsequently imaged again after 8 hours of growth (T8) (Figure 1A). Changes in cell length along the principal direction of growth were quantified using MorphoGraphX[32,33] (Figure 1B), and data were integrated into a correspondence matrix capturing mean elongation (strain) at discrete positions along the hook (Figure 1C). Along the longitudinal axis of the hook, we refer to the cotyledon-proximal domain as apical and the hypocotyl-proximal domain as basal. Along the radial axis of the hook, curvature establishes opposing inner (concave) and outer (convex) domains. Analysis within this quantitative framework, with the orthogonal apical–basal and inner–outer axes, revealed the spatial pattern of cell elongation that underlies hook maintenance (Figure 1B and C). Strain magnitudes differed between the inner and outer sides of the hook in both apical and basal regions, with maximal elongation occurring in the inner–basal region (Figure 1C and D). In the apical region,

cell elongation was higher on the outer side, whereas in the basal region, elongation was higher on the inner side (Figure 1C and D).

In agreement with previous reports[9], we observed an apical–basal displacement of cells across the hook midline over 8 hours of growth, giving rise to a net directional "flow" of cells through the curved organ (Figure S1A). Although apical hook curvature may appear to remain static during its maintenance, the constant flow of cells is highly dynamic and requires a positional- but not cell-dependent elongation program, where a single cell shows spatiotemporal-dependent rates of cell elongation, based on its relative position within the hook structure. These findings indicate that curvature maintenance arises not from static structural constraints but from the dynamic coordination of opposing growth fields across the hook.

To further investigate how spatial growth patterns translate into tissue-scale shape changes, we built an apical hook biomechanics solver using a two-dimensional finite element model (FEM) parameterized by cell-scale growth rates derived from our high-resolution dataset. Growth of each cellular domain on the apical hook 2D mesh was modelled using a distinct experimentally-derived strain rate tensor, defining a unique growth scheme for every cell, while strain-dependent growth shaped the extracellular domain. First, we simulated 8 hours of the hook maintenance phase using a reference mesh from a representative seedling (Figure 1E). Model benchmarking was performed by applying pooled seedlings growth parameters, reproducing observed curvature dynamics (Figure 1E, T8). It should be noted that these seedling representations are in only 2D, but they provide a simplified framework for simulating apical hook kinematics. Next, we simulated a perturbed local growth anisotropy by dissipating the elongation gradient in either the apical (Figure S1B) or basal (Figure S1C) domain with low and high uniform growth. Loss of the apical growth gradient while preserving the basal growth gradient led to progressive hook opening, whereas removal of the basal growth gradient with retention of the apical growth gradient exaggerated hook curvature (Figure 1F). The magnitude of growth within the uniform growth domain further modulated these effects: in the basal region, high uniform growth amplified over-hooking compared with low uniform growth, while in the apical region, higher growth resulted a greater decrease in curvature (Figure 1F).

Our simulations demonstrate that in a two-dimensional representation of the apical hook structure, a stable hook angle emerges from the dynamic equilibrium between two distinct and opposite "counter-gradients" of cell elongation that contribute antagonistically to organ curvature. Together with our quantitative imaging, this computational modelling approach directly connects cellular elongation patterns to apical hook-scale morphogenesis.

Cuticle integrity controls apical hook development

Computational simulations indicated that disrupting the balance between apical and basal counter-gradients should impair curvature stability. To better understand the factors coordinating the two opposing growth gradients on either side of the hook midline, we performed genetic perturbations guided by our modeling predictions. We used the *hookback* (*hkb)* mutants previously isolated from a forward genetic screen for defects in auxin-dependent apical hook development[34]. Among these, we selected two mutants, *hkb2* and *hkb4*, that displayed defects in apical hook maintenance under control conditions. Both mutants displayed a similar phenotype, presenting a normal formation phase, shorter maintenance phase, and earlier and faster hook opening than wild-type (WT) (Figure 2A). Whole genome sequencing revealed the presence of mutations in genes with roles in cuticle biosynthesis—the *CYTOCHROME P450, FAMILY 77, SUBFAMILY A, POLYPEPTIDE 4* (*CYP77A4)* gene in *hkb2* (G to A non-synonymous substitution at chromosome 5, position 1337420) and the *DEFECTIVE IN CUTICULAR RIDGES* (*DCR*) gene in *hkb4* (C-to-T non-synonymous substitution at chromosome 5, position 8077553)—suggesting a potential link between cuticle

function and apical hook development. To confirm that the identified mutations were responsible for this phenotype, we analyzed hook angle kinematics of the insertional mutants *cyp77a4-4* and *dcr-2*. Both displayed very similar phenotypes to *hkb2* and *hkb4*, with a shorter maintenance phase, as well as earlier and faster hook opening than WT (Figure 2A), suggesting that cuticle layer integrity is important for proper apical hook development. We further examined apical hook development in *cyp77a4-3* complemented with *pCYP77A4::CYP77A4-GFP* and in *dcr-2* complemented with *pDCR::DCR-mCherry* (Figure S2A,B). We observed that the *cyp77a4-3* allele displays a similar hook development pattern to *cyp77a4-4* and *dcr-2,* and that both complemented lines are rescued in apical hook development compared to the non-complemented mutants (Figure S2A, B). This confirms that the developmental defects of the mutants are attributable to loss of CYP77A4 or DCR function. We next investigated CYP77A4-GFP and DCR-mCherry expression patterns in the complemented lines. Remarkably, we observed a gradual increase in CYP77A4-GFP and DCR-mCherry protein abundance over time, with relatively minimal accumulation at the early maintenance phase (22-24 hours post germination), greater protein abundance at the maintenance phase (34-38 hours post germination) and highest abundance at the late maintenance phase (46-52 hours post-germination), suggesting a potentially developmentally regulated role of CYP77A4 and DCR in apical hook morphogenesis (Figure_S2C).

To establish whether the defects in apical hook development are linked to cuticle integrity defects in the mutants, we analyzed hook angle kinematics of four additional mutants of genes involved in cuticle biosynthesis or transport: *long-chain acyl-coA synthase 1* (*lacs1-1*), *glycerol-3-phosphate sn-2-acyltransferase 8* (*gpat8*), *atp-binding cassette g 11* (*abcg11-7*) and *bodyguard 1* (*bdg1-8*). While *lacs1-1* and *gpat8* exhibited a WT-like phenotype, *abcg11-7* and *bdg1-8* displayed a shorter maintenance phase as well as earlier and faster apical hook opening (Figure S2D), similar to *cyp77a4-4* and *dcr-2*. We also assessed cuticle integrity at the apical hook in these mutants by performing toluidine blue staining on two-day-old seedlings[35]. Toluidine blue is a cationic dye that is prevented from penetrating tissues by an intact cuticle; therefore, visible tissue staining is diagnostic of increased cuticular permeability. Those mutants displaying altered apical hook kinematics compared to WT also showed strong toluidine blue staining in the apical hook region, while no staining was observed for Col-0, *lacs1-1* or *gpat8* (Figure S2E), reinforcing the hypothesis that cuticle integrity is necessary for proper apical hook development.

To further confirm that cuticle integrity plays a role during apical hook development, and to assess whether the cuticle present on either side of the hook might play differential roles, we enzymatically impaired cuticle integrity by locally expressing the *CUTICLE DESTRUCTING FACTOR 1* (*CDEF1*) gene of *Arabidopsis*, encoding an esterase that degrades cutin polyester[36]. We expressed *CDEF1-mCherry* under the control of the *DCR* promoter, which is active throughout the apical hook epidermis[37,38], and the *SMALL AUXIN UP-REGULATED RNA (SAUR) 16* and *57* promoters, as they are specifically expressed in the inner or outer side of the hook, respectively[39] (Figure 2B). First, we confirmed that CDEF1-mCherry was expressed across the apical hook when driven by *pDCR* and enriched in the inner or outer sides when driven by the *pSAUR16* and *57* promoters, respectively (Figure 2B). We then verified the extent of cuticle integrity loss induced by CDEF1 activity with toluidine blue staining and found that the pattern of staining was comparable to the domain of CDEF1 expression (Figure 2B). The *CDEF1*-expressing lines displayed similar apical hook kinematics to *cyp77a4-4* and *dcr-2*, with a shorter maintenance phase and earlier and faster apical hook opening compared to WT control (Figure 2C). In particular, cuticle degradation across the whole hook region (under *pDCR*-driven expression) induced even earlier opening than observed in *cyp77a4-4*, *dcr-2* or the *pSAUR*-driven expressors of *CDEF1*, most probably due to the high activity of the esterase. No major differences could be observed between the lines

with loss of cuticle integrity in the inner or outer hook side. Overall, our results clearly indicate that cuticle integrity on both sides of the hook is essential for proper apical hook morphogenesis and that local loss of cuticle integrity likely acts in a non-cell autonomous fashion.

To analyze cuticular ultrastructure in the apical hook of our cuticle-affected lines, we performed transmission electron microscopy (TEM) in longitudinal sections of hooks in the maintenance phase (approximately 30 to 36 hours post-germination) (Figure 2D). In WT, the cuticular layer of the outer side of the hook is adjacent to the cell wall and appears as a diffuse longitudinal deposition. On the inner side, this layer appears thin and compact, coated by a thicker, electron-translucent layer of cuticle proper. Thus, the cuticle structure differs between the outer and inner side of the hook during the maintenance phase, suggesting that its status changes dynamically, likely in coordination with the cell growth rate. In the *cyp77a4-4* and *dcr-2* mutants, and most of the *CDEF1*-expressing lines, we showed an abundant opaque deposition on both the outer and inner sides, revealing qualitative disruptions in the deposition and/or organization of the cuticular layer in these lines. Taken together, these results confirm that the cuticle biosynthesis mutants are defective in cuticle ultrastructure and permeability, and establish these defects as the cause of the observed deficiency in apical hook maintenance.

Cuticle integrity regulates coordinated antagonistic growth dynamics

To further understand the cuticle's role in apical hook morphogenesis, we analyzed cell size in the apical hook region in Col-0 and the cuticle biosynthesis mutants stained with the cell wall dye propidium iodide (PI) at 24 hours after germination. We observed statistically significant reductions of ~12% and 18% in mean cell length in the outer apical hook region of *cyp77a4-4* and *dcr-2*, respectively, compared to WT (Figure S2F), implicating the cuticle in the regulation of cell and organ geometry. These data suggest a possible reduction in cell elongation rates or increased cell division frequency in *cyp77a4-4* and *dcr-2* compared to Col-0. To decipher between these two possibilities, we used light-induced acceleration of apical hook opening as a readout of cell elongation rates on the inner hook side[40]. The mutants *cyp77a4-4* and *dcr-2* displayed a statistically significant reduction in the rate of light-induced apical hook opening compared to Col-0 (Figure S2G), suggesting impaired differential cell elongation in the mutants.

We then performed time-lapse imaging on the *p35S::PIP2A-GFP* expressing lines in WT, *cyp77a4-4* and *dcr-2* backgrounds at T0 and T8 to directly observe the magnitude and distribution of cell expansion (Figure 2E, F). Notably, the PIP2A-GFP signal was weaker in the mutant backgrounds, but the cell outlines were still visible. Data were integrated into a correspondence matrix to spatially map cell expansion during apical hook maintenance in *cyp77a4-4* and *dcr-2* (Figure 2G). In these mutants, we observed a disruption in the counter-gradient system compared to WT (Figure 2F and G). Importantly, the apical counter-gradient was nearly abolished in *cyp77a4-4* and *dcr-2* during apical hook maintenance, while the basal gradient appeared to be weaker in comparison to that of WT (Figure S2H), suggesting that cuticle integrity is required for counter-gradient growth coordination during apical hook maintenance.

Using our biomechanical model (Figure 1E, F), we simulated the development of representative *cyp77a4-4* and *dcr-2* apical hooks constructed using data from the time-lapse experiments to predict mutant hook morphodynamics (Figure 3A, B). To understand if the mutants' disrupted counter-gradients sufficiently explain their hook development phenotype, we simulated the development of a WT reference mesh with each mutant's aggregated cell elongation data (Figure 3C). Under both the *cyp77a4-4* and *dcr-2* growth regimes, the WT reference mesh exhibited reduced hook angles at the end of the simulation compared with the control WT growth regime, which maintained stable curvature throughout the simulation (Figure 3B, C), suggesting that the disrupted counter-gradients in *cyp77a4-4* and *dcr-2*

sufficiently account for their defects in apical hook development. Compared to WT apical hooks, both *cyp77a4-4* and *dcr-2* display differences in cell geometry at the beginning of the maintenance phase (Figure S2F). To assess the impact of initial cell geometry, we simulated curvature maintenance using the WT growth regime in *cyp77a4-4* and *dcr-2* apical hook meshes. Applying WT growth patterns to the *dcr-2* geometry restored apical hook maintenance (Figure 3D); the *cyp77a4-4* geometry, however, displayed an exaggeration of hook curvature under a WT growth regime (Figure 3D), suggesting that initial tissue geometry also contributes to apical hook development dynamics. These simulations indicate that the absence of counter-gradient growth provides a strong morphomechanical basis for the premature hook-opening phenotype observed in cuticle-defective mutants.

ROS link cuticle permeability to the control of counter-gradients during apical hook maintenance

Increased cuticle permeability has been shown to be associated with elevated production of ROS[27,28,41], and ROS accumulation has been observed in the apical hook[42]. Using 3,3'-diaminobenzidine (DAB) staining[43], we observed elevated hydrogen peroxide levels in the apical hook of the mutants *dcr-2* and *cyp77a4-4* compared to WT (Figure 4A). To dissect the relationship between elevated ROS accumulation and coordinated growth necessary for apical hook maintenance, we utilized both pharmacological and genetic approaches. Diphenyleneiodonium (DPI) treatment inhibits the activity of NADPH oxidases and thereby ROS production[44]. We confirmed a DPI-induced reduction in hydrogen peroxide levels in *cyp77a4-4* and *dcr-2* hooks via DAB staining (Figure S3A) and observed that DPI prolonged the maintenance phase in both mutants compared to mock treatment, while having little effect on WT (Figure 4B). We also observed that the reduction in ROS accumulation under DPI treatment did not restore the cuticle permeability defect in the mutants (Figure S3B). The prolongation of hook maintenance in the mutants upon DPI treatment suggests a role for NADPH oxidase-mediated ROS production in regulating coordinated cell growth patterns. To confirm this, we analyzed apical hook development in plants overexpressing *PEROXIDASE71* (*p35S::PRX71*), which show increased ROS accumulation[45], as well as in the *respiratory burst oxidase homolog D (rbohD*) and *peroxidase71-1* (*prx71-1*) mutants, both of which exhibit reduced ROS accumulation in response to isoxaben treatment[45]. Notably, *p35S::PRX71* displayed a shortened maintenance phase and premature apical hook opening compared with WT (Figure 4C), further supporting a role for ROS in the regulation of apical hook development. The *rbohD* and *prx71-1* mutants displayed similar hook development kinematics to WT (Figure 4D, E and F). To assess the effect of genetic inhibition of ROS production in the cuticle mutants, we attempted to cross *rbohD* and *prx71-1* with each of *dcr-2* and *cyp77a4-4*. We were unable to obtain the double-homozygous *dcr-2 rbohD* line, most likely due to an embryo lethality issue (Figure S3C). Interestingly, the double mutants *cyp77a4-4 rbohD, dcr-2 prx71-1* and *cyp77a4-4 prx71-1* all displayed a prolongation of the maintenance phase compared to the single cuticle mutants (Figure 4D, E and F). Taken together, these results show that elevated ROS accumulation destabilizes organ curvature, indicating that ROS levels regulate morphogenetic growth processes.

Loss of cuticle integrity disrupts the mechanical conditions required for curvature stability

Cell expansion is driven by the biomechanical feedback between turgor pressure and a structurally anisotropic cell wall, the extension and extensibility of which is directed and dynamically regulated by mechanical stress patterns and regulators of cell wall structure and composition[6,46–50]. The observed changes in differential growth patterns at the apical hook in *cyp77a4-4* and *dcr-2* prompted us to assess the potential involvement of the cuticle in

regulating the biomechanics of cell growth. We used atomic force microscopy (AFM) to directly quantify cell wall indentation stiffness, and since our cell elongation data was recorded in the *p35S::PIP2A-GFP* background, we used the same lines for the AFM experiments. Technical difficulties made it unfeasible to perform these experiments directly in the apical hook; however, we observed that the base of the hypocotyl also displayed significantly shorter cells in *cyp77a4-4* and *dcr-2*, with a ~20% reduction in mean cell length, compared to WT background (Figure S4A–B), making this region relevant for AFM measurements. We observed that the mean cell wall indentation stiffness (Young's modulus) in the basal region of Col-0 background hypocotyls was significantly different to that of the mutants, being around 12% higher than in *cyp77a4-4* and *dcr-2* backgrounds (Figure 5A), demonstrating that a disruption of cuticle integrity results in changes in tissue biomechanics.

To verify that the observed differences in indentation stiffness were biologically significant, we visualized subcellular fluorescent markers known to be responsive to mechanical stress patterns. Cortical microtubule organization is known to respond to tissue-scale mechanical stress patterns, aligning with the direction of maximal tensile stress[51–54]. We imaged the outer face of epidermal cells in apical hooks of the cortical microtubule marker line *p35S::GFP-MBD* in Col-0 x Ws-4, *cyp77a4-4* and *dcr2* backgrounds and analyzed microtubule organization. Compared to WT background, the mutants *cyp77a4-4* and *dcr-2* displayed statistically significant hyper-alignment of cortical microtubules (Figure 5B and C), with approximately 26% and 8% higher mean anisotropy respectively, reflecting altered mechanical stress patterns in the mutants.

Sites of tissue compression in the shoot apical meristem boundaries display deformed nuclei consistent with the extent of organ growth[55], demonstrating that the shape of the nuclear envelope reflects tissue-scale mechanical stress patterns. We observed the nuclear envelope marker *p35S*::*SUN1-YFP* in apical hooks of WT, *cyp77a4-4* and *dcr*-2 backgrounds and quantified nuclear shape as the aspect ratio between height and width, with 1 indicating a perfect circle, and higher values indicating an increasingly deformed shape. The mean aspect ratio of nuclei in the apical hooks of all lines was significantly different between the outer and inner hook sides (Figure 5D-G). The Col-0 mean nuclear aspect ratio was 15% higher in the outer compared to the inner side, while in *cyp77a4-4*, the mean aspect ratio of nuclei was only 12% higher on the outside compared to the inside (Figure 5D and E). Furthermore, the mean aspect ratio of nuclei in *cyp77a4-4* was lower by 8% and 11% on the inside and outside respectively compared to the corresponding Col-0 nuclei. A very similar trend was also observed *in dcr-2* (Figure 5F and G). Overall, we observed that increased cuticle permeability is associated with rounder nuclei on average, strengthening the idea that cuticle integrity plays a role in regulating and redistributing mechanical stress patterns.

Previous studies have demonstrated that reducing the water potential of solid growth media by increasing agar concentration results in reduced epidermal tension and apparent cell wall stiffness[51]. Further, increased agar concentration has been shown to rescue apical hook developmental defects in cell wall integrity-affected mutants[56]. We tested the relationship between cuticle integrity and cell wall biomechanics under altered water availability by monitoring hook development in WT, *cyp77a4-4* and *dcr-2* when grown on medium with high agar concentration (2.5% w/v, hereafter referred to as high-agar or HA), compared to medium with our usual agar concentration (0.8% w/v, also referred to as low-agar or LA). WT apical hooks opened 6–9 hours earlier on HA compared to LA (Figure 5H). Interestingly, mean *dcr-2* and *cyp77a4-4* apical hook angles were >30% higher on HA than LA after 48 hours of growth (Figure 5H). Importantly, growth on HA did not rescue the cuticle integrity defects of the mutants, as seen with toluidine blue staining (Figure S4C), suggesting that the observed rescue of *dcr-2* and *cyp77a4-4* apical hook curvature on HA is independent of cuticle integrity. When grown on HA medium, hypocotyls of *p35S::PIP2A-GFP* in the Col-0 background displayed a

significant 27% reduction in mean indentation stiffness of the epidermal cell walls measured using AFM, bringing the stiffness to a level statistically indistinguishable from the *cyp77a4-4* and *dcr-2* backgrounds grown on HA medium (Figure 5I). The apparent indentation stiffness remained unchanged in the *cyp77a4-4* and *dcr-2* mutants grown on HA compared to LA (Figure 5I); however, the shift in apical hook kinematics observed in *cyp77a4-4* and *dcr-2* (Figure 5H) shows that the mutants are sensitive to changes in water potential. Analysis of the differential cell growth patterns over 8 hours (at T0 and T8) in apical hooks of *p35S::PIP2A-GFP* in Col-0, *cyp77a4-4* and *dcr-2* backgrounds grown on HA revealed an apparent restoration of the counter-gradients in the cuticle biosynthesis mutants (Figure S4D and Figure 5J–K) compared to when grown on LA (Figure 2F–G). Taken together, these results suggest a biomechanical link between cuticle integrity and curvature stability.

Biomechanical cues link ROS levels with curvature stability

The observed stabilization of apical hook curvature in *cyp77a4-4 and dcr-2* when grown on HA prompted us to investigate whether ROS accumulation was sensitive to changes in agar concentration. Interestingly, DAB staining revealed reduced ROS levels in *cyp77a4-4* and *dcr-2* when grown on HA compared to LA (Figure 6A). Taking into account the permeable cuticle of these mutants, these results suggest that ROS accumulation occurs downstream of putative biomechanical factors.

To assess whether these biomechanical factors are cuticle integrity-specific, we investigated apical hook kinematics and ROS levels in LA and HA growth conditions in cell wall-affected mutant lines previously characterized for defective hook maintenance, which are known to be rescued under HA conditions[56]. The selected mutants, *quasimodo2-1* (*qua2-1*), *glucuronate 4-epimerase1* and *6* (*gae1-1 gae6-1*) and *murus1* (*mur1-3),* are defective in pectin biosynthesis. Consistent with previous reports, all of the mutants exhibited defective hook maintenance under LA conditions, and the defect was partially rescued under HA conditions (Figures 6B–D). When grown on LA, the cell wall-affected mutants also exhibited elevated ROS levels compared to WT (Figure 6E). In HA conditions, however, ROS accumulation was reduced in all the mutants (Figure 6E), suggesting that organ curvature stability is orchestrated by ROS levels acting downstream of biomechanical factors that integrate cuticle and cell wall integrity.

Together, our work demonstrates that organ morphogenesis is not merely driven by growth promotion or repression, but is a highly dynamic, tightly regulated process where ROS integrate biomechanical signals to coordinate growth patterns, thus shifting the paradigm for how we understand morphogenesis.

Discussion

Our study makes a compelling addition to the mounting pool of evidence[9,30,57] that a pair of opposing gradients of anisotropic cell growth form the core mechanism sustaining apical hook curvature during the maintenance phase. Differential growth has long been implicated in hook morphogenesis[58], with relatively straightforward, unidirectional cell elongation gradients driving the formation and opening phases of apical hook development[15,41,59,60]. Here we show that apical hook maintenance is a more complex process requiring the continuous coordination of a pair of opposing cell elongation gradients. This counter-gradient principle represents a conceptual advance over classical models that proposed a transition between differential growth repression and promotion at the inner side to explain hook shape. Although antagonistic growth zones were previously proposed based on kinematic and physiological observations[9,13,29–31], direct quantitative evidence at cellular resolution has only begun to emerge recently (this study and [57]). By integrating time-resolved imaging with mechanical modeling, we demonstrate that apical hook maintenance emerges as a direct mechanical consequence of these antagonistic growth gradients. Selective dissipation of growth anisotropy

in either apical (such as in *cyp77a4-4* and *dcr-2* mutants) or basal domains was sufficient to destabilize hook shape, driving premature opening or exaggerated curvature, respectively. Our findings further suggest that transitions between hook formation, maintenance, and opening are regulated by rebalancing pre-existing growth fields rather than by abrupt switches in growth programs. Such a mechanism provides robustness while preserving developmental flexibility, allowing rapid modulation of hook curvature in response to environmental cues. More broadly, counter-gradient growth dynamics may represent a general principle of plant morphogenesis, enabling the stabilization of curved or asymmetric forms while maintaining the capacity for rapid growth and shape changes in diverse developmental contexts.

Although traditionally regarded as a protective barrier (such as in the root cap[19]), the plant cuticle has increasingly been implicated in the regulation of growth and tissue mechanics[21]. While the cuticle-defective *cyp77a4-4* and *dcr-2* mutants underwent a normal formation phase, indicating that cuticle integrity is dispensable for the initial establishment of growth asymmetry, disruption of cuticle integrity at later stages selectively impaired hook maintenance, which uncouples the establishment and maintenance of differential growth. This loss of curvature correlated with altered antagonistic growth gradients, demonstrating that sustained differential growth requires an intact cuticle. The accumulation of CYP77A4 and DCR during the maintenance phase indicates that CYP77A4- and DCR-dependent cuticle biosynthesis is tightly developmentally regulated. These results uncover a phase-specific role for the cuticle, positioning it as a key mechanical and regulatory component that preserves growth asymmetry after it has been established, rather than contributing to its initial formation. In line with previous observations that cuticle-defective mutants display reduced cell elongation in etiolated hypocotyls and elevated activity of the cell cycle regulator CYCLIN B1 (CYCB1) in root and shoot apices[38,61], we observed a general reduction in cell expansion rates and anisotropy in cuticle-deficient apical hooks. These effects lead to a pronounced attenuation of the antagonistic growth gradients required for curvature maintenance. Mechanical simulations further support the conclusion that altering growth dynamics is sufficient to destabilize hook curvature irrespective of initial tissue geometry, highlighting the importance of cuticle integrity for coordinating spatial growth patterns. The sensitivity of anisotropic growth patterns and organ biomechanics to water potential further highlights the cuticle's importance to cell, tissue and organ-scale biomechanics. Cuticle-mediated developmental regulation has also been implicated in other contexts, such as in petal and embryo development, where cuticle integrity contributes to proper tissue patterning and prevents organ fusion, consistent with a role in coordinating growth across tissues[62,63]. Together with studies of expanding organs such as tomato fruit, which demonstrate that cuticle mechanical properties are developmentally regulated and spatially heterogeneous[64–67], these findings support a broader view of the cuticle as a structural component that contributes to the mechanical framework underlying coordinated growth and morphogenesis across plant development.

Perturbations in cell wall integrity trigger ROS production as part of a tightly regulated compensatory and signaling response. Altered wall architecture, such as reduced cellulose or pectin integrity, is sensed by cell wall integrity-monitoring pathways involving receptor-like kinases such as THESEUS1 and FERONIA, which initiate downstream ROS-generating mechanisms[68,69]. Additionally, FERONIA nanodomain assembly is sensitive to extracellular osmotic status[70]. ROS production occurs through both NADPH oxidases and Class III peroxidases (CIII Prxs), providing spatially localized oxidative signals that reinforce wall structure and modulate growth[71]. In the *Arabidopsis* root, mechanical stretching induces NADPH oxidase-mediated ROS production, resulting in cell wall reinforcement[25], which links ROS signaling with biomechanical response and regulation. Further, the peroxidase PRX71 is upregulated in response to cell wall damage and mediates ROS accumulation in *Arabidopsis*[45]. Loss-of-function mutants of *PRX71* partially suppress the ROS burst and the associated growth

inhibition observed in cell wall–defective mutants, indicating that peroxidase-mediated ROS are essential effectors of the compensatory response. PRX-dependent ROS contribute to oxidative cross-linking of wall polymers and localized lignification, reinforcing tissue mechanics and restricting abnormal expansion. Together, these studies establish ROS as central mediators linking cell wall integrity defects to adaptive growth and developmental responses. In the context of apical hook development, this suggests that cuticle integrity may similarly interact with ROS-mediated mechanical feedback: defects in the cuticle or cell wall could perturb local tissue mechanics and potentially osmotic homeostasis, influencing growth gradients and the maintenance of organ curvature, analogous to the effects observed with cell wall defects and peroxidase-dependent ROS. While diverse environmental or developmental cues can activate distinct signaling pathways, they may converge in ROS production, which is known to influence cell wall properties, directional cell expansion, and cortical microtubule dynamics[72]. One example of this is the recent work showing that osmotic stress triggers ROS accumulation through a ROP6-dependent pathway activated by the guanine nucleotide exchange factor GEF14, which organizes stimulus-specific ROP6 nanodomains at the plasma membrane[73]. In this framework, the reduced growth anisotropy and attenuation of antagonistic growth gradients in cuticle-defective apical hooks may be consistent with altered ROS-mediated control of directional growth at the cellular level. Although these links remain speculative, they would suggest that the cuticle can support tissue-scale morphogenesis by modulating the capacity of epidermal cells to generate and maintain coordinated, anisotropic growth patterns.

Material and methods

Plant material and growth conditions

All *Arabidopsis thaliana* mutants and transgenic lines were in Columbia-0 (Col-0) ecotype background except *p35S::GFP-MBD* which was in Ws-4 background. *Arabidopsis* lines *dcr-2* (SALK_128228), *cyp77a4-3 pCYP77A4::CYP77A4-GFP*, *lacs1-1* (SALK_127191), *abcg11-7* (+/-) (GABI_590C03), *gpat8* (SALK_035914), *p35S::PIP2A-GFP*, *p35S::GFP-MBD*, *p35S::SUN1-YFP*, *qua2-1*, *gae1-1 gae6-1*, *mur1-3, rbohD* (NASC: N9555), *prx71-1* (SALK_123643) and *35S::PRX71* were described previously[37,38,45,55,74–84]. The *Arabidopsis* lines *bdg1-8* (SM_3_24890), *cyp77a4-3* (SALK_112368C) and *cyp77a4-4* (SALK_092049C), were obtained from the publicly available library at NASC[85]. The selection of *hkb2* and *hkb4* was previously described [34]. The *cyp77a4-4 p35S::PIP2A-GFP, dcr-2 p35S::PIP2A-GFP, cyp77a4-4 p35S::SUN1-YFP*, *dcr-2 p35S::SUN1-YFP*, *cyp77a4-4 p35S::GFP-MBD, dcr-2 p35S::GFP-MBD*, *dcr-2 prx71-1* and *cyp77a4-4 rbohD* lines were generated by crossing. The homozygotes were screened using fluorescence and PCR genotyping, which was performed by extracting template DNA extracted as previously described[86], followed by PCR amplification using primers in Table S1 for insertional mutants. Because *p35S::GFP-MBD* was in the Ws-4 background, F_2 generation seedlings obtained from the cross between *p35S::GFP-MBD* and *dcr*-2 were screened for fluorescence, and seedlings that genotyped as wild-type for *DCR* were chosen as the control line (Col-0 x Ws-4). *pSAUR16::CDEF1-mCherry*, *pSAUR57::CDEF1-mCherry* and *pDCR::CDEF1-mCherry* in the *p35S::PIP2A-GFP* (Col-0) background, and *dcr-2 pDCR::DCR-mCherry* lines were produced in this study.

Seeds were surface sterilized for two minutes with a solution of 70% ethanol and 1% Tween 20, then washed twice with 95% ethanol and left drying under a sterile hood before sowing on square Petri plates (12x12 cm) of growth medium (GM) composed of half strength Murashige and Skoog (MS) medium (Duchefa Biochemie, Haarlem, The Netherlands), 0.05 % morpholinoethanesulfonic acid (Sigma-Aldrich), 1 % sucrose and 0.8 % agar (Duchefa Biochemie), at pH 5.7. Seeds were placed at 4ºC for two to four days and then transferred to 22ºC for 16/8 hours of light/darkness per day, or for six hours of light before wrapping in aluminium foil for dark growth. For kinematics of apical hook development, after six hours of light treatment, plates were placed vertically in a dark box equipped with infrared lights (940 nm) (SOLAROX®) and photographed with Raspberry Pi NoIR v2 cameras controlled by Raspberry Pi 3 Model B+ computers. For time-lapse cell length quantification, seedlings were germinated in Petri plates and then transferred to 3D printed square black plates using PETG filaments containing half strength MS medium. After the transfer, one drop of 1% low melting agar (Invitrogen™ UltraPure™ Low Melting Point Agarose) was added at the bottom of the hypocotyl to maintain the seedlings in place.

Chemical treatment

A 3 mM stock solution of diphenylene iodonium chloride (DPI; Sigma-Aldrich) was prepared in dimethyl sulfoxide (DMSO) and added to half-strength MS medium at the indicated concentrations during plate preparation. Control medium contained an equivalent volume of DMSO for comparison.

Sequencing EMS mutants

The *hkb2* and *hkb4* mutants were backcrossed twice with Col-0. Genomic DNA extraction and whole genome sequencing were performed as described previously[34]. The sequencing raw data has been deposited at the European Nucleotide Archive (ENA), https://www.ebi.ac.uk/ena (accession number: PRJEB87260).

Generation of transgenic plants

For all the cloning, DNA amplification by PCR was performed using Phusion High-Fidelity polymerase (Invitrogen), which was then inserted into GreenGate vectors using methods previously described[87]. The promoter of DCR (2930 bp), SAUR16 (2574 bp) and SAUR57 (3231 bp) were amplified with the following primers: proDCR-F and proDCR-R; proSAUR16-F and proSAUR16-R; proSAUR57-F and proSAUR57-R respectively, and the products were inserted into the pGGA000 vector. The CDEF1 coding sequence (1044 bp) was amplified using CDEF1-F and CDEF1-R primers; the DCR coding sequence (1452 bp) was amplified using DCRFwGG and DCRRevGG, and both the products were inserted in the pGGC000 vector. The primer sequences are listed in Table S1.

The entry vectors were used to generate *pDCR::CDEF1-mCherry*, *pSAUR16::CDEF1-mCherry*, *pSAUR57::CDEF1-mCherry* and *pDCR::DCR-mCherry* binary destination vectors. Stable transformation of *Arabidopsis* mediated by *Agrobacterium tumefaciens* was performed by floral dip[88]. Transformants were selected on hygromycin and homozygous T3 lines were confirmed by the presence of fluorescence in all screened seedlings.

Toluidine blue staining

Toluidine blue O (Sigma 198161) staining was performed as previously described[35]. Briefly, seedlings were transferred to wells of a multi-well-plate containing 0.1% toluidine blue water solution for two minutes and then washed in distilled water. Seedlings were mounted in water on glass slides with coverslips and images were acquired with a Zeiss Axioplan 2 microscope equipped with a color camera using AxioVision software. Identical settings were used for acquisition of all images. For figures S3C and S4B, four to five images of slightly different focal planes were taken for each seedling, which were then processed in Photoshop software to enhance the focus of the final image as follows: the images were aligned using the "auto-align layers" function, before converting to a "smart object" and stacking using the "minimum" mode. For figures 2B and S2E, a single image at a single focal plane was taken and subsequently cropped to size using ImageJ.

Propidium iodide (PI) staining

PI staining (Sigma-Aldrich P4170) was performed to visualize cell walls. Etiolated seedlings (48 hours) were incubated in a freshly prepared PI solution (10 µg/mL ½ MS liquid medium) for 15 mins for Col-0 and 1 minute for *cyp77a4-4* and *dcr-2* at room temperature. Following staining, seedlings were rinsed in ½ MS liquid medium. Seedlings were mounted on glass slides with water and cover slip and Z-stack images were acquired with the Zeiss LSM800.

3,3'-Diaminobenzidine (DAB) staining

DAB staining was performed as described previously[89]. The DAB staining solution was prepared by adding 1 mg/ml DAB (Sigma-Aldrich) to sterile water with stirring and 0.2 M hydrochloric acid (HCl) was added drop-wise to bring the pH of the staining solution to 3.0. Subsequently, 25 µl TWEEN® 20 (0.05% v/v) and 2.5 ml 200 mM Na_2HPO_4 were added to the solution, with continuous stirring. 2 ml of the DAB staining solution was transferred per well to a 12-well plate, and seedlings were incubated in the solution for 6–7 hours with shaking at 80–100 rpm. 10 mM Na_2HPO_4 solution was used as a control. Following the incubation, the staining solution was replaced with clearing solution (ethanol:acetic-acid:glycerol in a 3:1:1 ratio) and the plate was incubated at 65°C for 15 minutes. The bleaching solution was then replaced with fresh bleaching solution and the plate was allowed to stand at room temperature for 30 minutes. The apical hook region was directly visualized for DAB staining under a Leica DMi8 microscope.

Confocal microscopy

For time-lapse cell length quantification, lines expressing *p35S::PIP2A-GFP* were imaged with a ZEISS LSM800 confocal microscope using the W N-Achroplan 20x/0.5 water-immersion objective, and samples were excited with a 488 nm wavelength laser. Z-stacks were acquired with a step-size of 1 µm, with the stack extending from slightly above the epidermis to the stele. Seedlings were imaged at 2 time-points in an 8-hour interval during the maintenance phase. The first time-point was approximately 24–28 hours after germination, and the second time point was approximately 32–36 hours after germination.

For CYP77A4, DCR and CDEF protein localization, seedlings were mounted on glass slides with liquid half-strength MS medium supplemented with 1% sucrose at pH5.7. Confocal Z-stacks were acquired using a ZEISS LSM800 confocal microscope equipped with a C-Apochromat 40x/1.20 water-dipping objective, and the seedlings were excited with a laser of wavelength 488 nm (*pCYP77A4::CYP77A4-GFP*), 587 nm (*pDCR::DCR-mCherry*) or 561 nm (*pSAUR16::CDEF-mCherry*, *pSAUR57::CDEF-mCherry* and *pDCR::CDEF-mCherry)*.

For lines expressing *p35S::MBD-GFP* and *p35S::SUN1-YFP*, images were acquired with a ZEISS LSM800 confocal microscope using the W Plan-Apochromat 40x/1.0 differential interference contrast (DIC) water-immersion objective, and samples were excited using a 482 nm laser (GFP) or a 508 nm laser (YFP). Z-stack step-size was set to 0.62 µm, with the stacks spanning from slightly above the epidermis to the stele.

For PI staining, fluorescence imaging was performed using a ZEISS LSM800 using the W Plan-Apochromat 40x/1.0 differential interference contrast (DIC) water-immersion objective confocal microscope with excitation at 561 nm and emission detected from 600 nm. Z-stacks were acquired with a Z-step of less than 1 µm, covering the top to the middle of the hypocotyl.

Image analysis

For quantification of apical hook development, the angle between the cotyledons and the hypocotyl was measured using the angle tool in ImageJ as described previously[10,11]. Hook angles were measured once every 3 hours, with the point of germination considered as hour 0. For cell length quantification after PI staining, Z-stack images were processed with SurfCut2 [90]to isolate the epidermal signal from propidium iodide (PI) staining. Two-dimensional projections were contrast-enhanced and subjected to Gaussian blurring to improve segmentation accuracy. When necessary, cell borders were manually reinforced using the pencil tool in ImageJ. Cell segmentation was carried out using MorphoLibJ [91], and cell length was quantified with the *Fit Ellipse* function in ImageJ. For quantification of cell growth patterns using live, time-lapse imaging, the acquired images were processed using MorphoGraphX as described previously[32].

To analyse spatial growth patterns within the apical hook and generate correspondence matrices, each cell centroid was transformed into a hook-centred polar coordinate system. A reference centre point was manually positioned at the inner curvature of the hook, and the position of every cell centroid was then expressed in polar coordinates, defined by radius (r) and angle (θ) relative to this point. To capture the overall geometry of the hook, a smooth spline was fitted to the relationship between r and θ, thereby defining the medial axis of the structure. Each cell was subsequently assigned a position along this medial axis based on arc length. The arc-length values were linearly rescaled to a range from 0 to 10, defining the basal-apical coordinate system, where 0 corresponds to the basal region of the hook and 10 corresponds to the apical tip. A second coordinate, termed the inner–outer axis, was calculated from the radial distance of each cell to the medial axis (spline). Lower values represent cells located on the inner (concave) side of the hook, whereas higher values correspond to cells positioned on the outer (convex) side. For spatial averaging and finite element model (FEM) input generation,

the continuous coordinates were discretised into a regular 8 × 8 positional grid. The basal–apical and inner–outer coordinate values were floored to integers and constrained to the interval [1, 8]. Cells from each seedling were assigned to bins based on their relative position along each axis, and the mean elongation rate was computed per bin across all seedlings, such that each bin in the final matrix reflects a population-level average for that spatial position. Code for this analysis is available with the FEM modelling repository (see corresponding methods section below). Microtubule orientation and anisotropy was quantified using the SurfCut2, Segmentation4FTBatch, FibrilTool, Cell_AspectRatio and Angle2Cell plug-ins for ImageJ (v1.54f)[92] using the workflow described previously[93,94]. Briefly, the confocal stacks were processed with SurfCut2 to separately extract the cell boundaries and microtubule signals. The cell boundaries were subsequently segmented using the Segmentation4FTBatch macro. FibrilTool was subsequently used to quantify microtubule organisation. The Cell_Aspect_Ratio macro was then used to define the cell axes, following which the Angle2Cell macro was used to express microtubule organisation in relation to the cell axis. The anisotropy values were then extracted from the output of the final macro. All the macros used in this work have been adapted from the MT_Angle2Ablation_Workflow repository used by Demes and Verger[94], (https://github.com/VergerLab/MT_Angle2Ablation_Workflow). The adapted versions of the macros can be found at https://github.com/SRobertGroup/Fibril_Tool_Workflow_Raggi-et-al. For the quantification of nuclear shape, acquired Z-stack images were processed using FIJI (ImageJ v1.54f). In brief, Z-projections of acquired confocal images were generated, following which the polygon tool was used to manually demarcate nuclear boundaries. ~50 nuclei of epidermal cells of the apical hook were outlined per seedling. The ROI (regions of interest) analysis tool built into FIJI was used to calculate the aspect ratio (ratio of primary to secondary axis length) of the best-fit ellipses that followed the manually defined outlines using the "Fit Ellipses" and "Shape Descriptors" measurement options.

Transmission electron microscopy

The protocol for transmission electron microscopy was adapted from previously described protocols[19,95]. With a sharp razor blade, the apical hooks of thirty-hour-old seedlings were separated from the hypocotyl and gently transferred into a 2 mL tube containing 2.5% glutaraldehyde solution in 0.1M phosphate buffer (PB) pH 7.4 fixative for 1 hour at room temperature. After removing the fixative, 1-hour post fixation was performed in 1.5% osmium tetroxide and 1.5% potassium ferrocyanide in water. For sample dehydration, the following series was used: 30% ethanol 15 minutes, 50% ethanol 15 minutes, 70% ethanol 15 minutes, and 100% ethanol 15 minutes twice. Spurr resin (TAAB Laboratories, Aldermaston, England) infiltration was then performed with 33% resin in ethanol for 2 hours, 66% resin in ethanol for 2 hours, and finally 100% for 8 hours twice. Single hooks were aspirated with a plastic Pasteur pipette and placed at the bottom of an embedding capsule (TAAB Laboratories, Aldermaston, England) and 100% fresh spurr resin was added on top of the sample, filling the capsule. Samples were polymerized at 60 °C for 24 hours. 70 nm ultrathin sections were cut and then picked up on copper grids and examined with a Talos L120C transmission electron microscope (FEI, Eindhoven, The Netherlands) operating at 120 kV. Micrographs were acquired with a Ceta 16M CCD camera (FEI, Eindhoven, The Netherlands) using Velox ver 2.14.2.40.

Atomic force microscopy (AFM)

Samples were mounted on a small petri dish with a thin layer of FLEXBAR Reprorubber® Thin Pour Material (Flexbar Machine Corporation) to ensure sample immobilization without covering the sample surface. Once the layer was solidified, the samples were immersed in water. The AFM experiments were performed using a NanoWizard® 4 XP BioScience AFM

(Bruker) equipped with HybridStageTM controlled by JPK SPMControl Software version 7. The petri dish was placed on the AFM stage and the bottom part of the hypocotyl was localized using the brightfield optical system and camera of the microscope. Direct AFM measurements in the apical hook region were technically challenging as the cotyledons prevented the samples from lying completely flat and interfered with cantilever approach during acquisition. A low-resolution Quantitative Imaging™ (QI) map with an image size of 90 × 180 µm and a resolution of 45 × 90 pixels (2 µm per pixel) was acquired on the hypocotyls to identify the cells for Young's modulus measurements. Once the cells were visible on the QI map, the mode of the AFM was switched to Contact Force Spectroscopy and 30-40 measurement points were defined per cell, following which the force spectra measurements were recorded. Two regions of interest were acquired using QI mode for each hypocotyl per genotype per biological replicate. Three biological replicates were performed. The experiments were conducted in water at room temperature using biosphere B500-NCH cantilevers, which have a spring constant of 40 N/m and a tip diameter of 0.5 µm, with a sphere, Diamond-Like-Carbon tip. The cantilever calibration was done using a pre-calibrated method in JPK SPMControl Software version 7. The QI maps were acquired with the following settings: setpoint 500 nN, pixel time 65 ms, Z length 4.5 µm, speed 173.08 µm/s and all Contact Mode Force Spectra measurements were recorded with the following settings: setpoint 600 nN, Z Length 2 µm, and the Z Speed 1 µm/s. Contact Mode Force Spectra measurements were analyzed using the JPK Data Processing Software. To extract the apparent Young's modulus, the following functions were applied on the measurements: calibration, baseline subtraction, contact point and vertical tip position. The Hert/Sneddon model was first fitted to the entire force-depth curve and then refitted within the ∞ -100 indentation range using following settings: spherical tip shape, 500 nm tip radius and 0.5 Poisson's ratio. Once the apparent Young's modulus values were obtained, one mean value was calculated for each cell.

Finite element model (FEM)

To investigate the biomechanical relationship between local cell expansion patterns and apical hook morphogenesis, a two-dimensional finite element model (FEM) of the apical hook was developed, that simulates morphoelastic growth dynamics. The model was implemented in BVPy, a Python library based on FEniCS, which enables the numerical solution of partial differential equations using FEM. The model geometry was reconstructed from MorphoGraphX and projected on a 2D surface, segmented into cellular and extracellular domains. Each cellular domain corresponded to one biological cell, while the extracellular space represented the shared anticlinal walls of neighboring cells in a 2D projection. Growth was described by assigning a strain rate tensor to each cellular domain, derived from experimentally measured growth patterns. This allowed each cell within the mesh to express a unique, anisotropic growth scheme consistent with observed expansion behavior. The extracellular domain exhibited strain-dependent growth, coupling deformation with local mechanical stress to represent the passive mechanical response of the cell wall matrix. To account for spatial mechanical heterogeneity, two regional variations in Young's modulus were defined. These differences reflected the contribution of anticlinal walls to the overall stiffness of the 2D tissue representation. Poisson's ratio (0.4) was assumed to be constant across the tissue domain. Growth and deformation were coupled using a morphoelastic formulation based on the St. Venant–Kirchhoff hyperelastic material model. Dirichlet boundary conditions were applied by fixing the basal region of the hook to prevent translation or rotation, allowing deformation to occur only in the upper tissue regions. The FEM solver computed the equilibrium displacement field at each iteration with a time resolution of 2.4 min over 8 hours. Code available at: https://zenodo.org/records/20327637

Statistical analysis

Statistical analyses were performed in R (v4.5.1). For the analysis of growth gradients, he effect of genotypes, domains, and their interaction on observations were tested using two-way linear model fitted with the "*stats*" package. Adjusted means for all combinations were computed using "*emmeans*" package. Multiple comparisons among these combinations were summarized using a compact letter display generated with the "*multcomp*" package, with Šidák correction applied. For other statistical analyses, a one-way ANOVA followed by Tukey's *post-hoc* test ("*stats*" package) or a non-parametric Kruskal-Wallis followed by Dunn's test ("*FSA*" package). The cldList function ("*rcompanion*") was used to generate a compact letter display to summarise pairwise comparisons when Dunn's test was used.

References

1. Geitmann, A., and Ortega, J.K.E. (2009). Mechanics and modeling of plant cell growth. Trends in Plant Science *14*, 467–478. https://doi.org/10.1016/j.tplants.2009.07.006.

2. Bidhendi, A.J., and Geitmann, A. (2016). Relating the mechanics of the primary plant cell wall to morphogenesis. J Exp Bot *67*, 449–461. https://doi.org/10.1093/jxb/erv535.

3. Cosgrove, D.J. (2016). Plant cell wall extensibility: connecting plant cell growth with cell wall structure, mechanics, and the action of wall-modifying enzymes. J Exp Bot *67*, 463–476. https://doi.org/10.1093/jxb/erv511.

4. Cosgrove, D.J. (2024). Plant Cell Wall Loosening by Expansins. Annual Review of Cell and Developmental Biology *40*, 329–352. https://doi.org/10.1146/annurev-cellbio-111822-115334.

5. Delmer, D., Dixon, R.A., Keegstra, K., and Mohnen, D. (2024). The plant cell wall—dynamic, strong, and adaptable—is a natural shapeshifter. Plant Cell *36*, 1257–1311. https://doi.org/10.1093/plcell/koad325.

6. Majda, M., Grones, P., Sintorn, I.-M., Vain, T., Milani, P., Krupinski, P., Zagórska-Marek, B., Viotti, C., Jönsson, H., Mellerowicz, E.J., et al. (2017). Mechanochemical Polarization of Contiguous Cell Walls Shapes Plant Pavement Cells. Developmental Cell *43*, 290-304.e4. https://doi.org/10.1016/j.devcel.2017.10.017.

7. Majda, M., and Robert, S. (2018). The Role of Auxin in Cell Wall Expansion. International Journal of Molecular Sciences *19*. https://doi.org/10.3390/ijms19040951.

8. Jonsson, K., Ma, Y., Routier-Kierzkowska, A.-L., and Bhalerao, R.P. (2023). Multiple mechanisms behind plant bending. Nat. Plants *9*, 13–21. https://doi.org/10.1038/s41477-022-01310-y.

9. Raz, V., and Ecker, J.R. (1999). Regulation of differential growth in the apical hook of Arabidopsis. Development *126*, 3661–3668. https://doi.org/10.1242/dev.126.16.3661.

10. Žádníková, P., Petrášek, J., Marhavý, P., Raz, V., Vandenbussche, F., Ding, Z., Schwarzerová, K., Morita, M.T., Tasaka, M., Hejátko, J., et al. (2010). Role of PIN-mediated auxin efflux in apical hook development of Arabidopsis thaliana. Development *137*, 607–617. https://doi.org/10.1242/dev.041277.

11. Ma, Q., Liu, S., Doyle, S.M., Raggi, S., Pařízková, B., Barange, D.K., Ratnakaram, H., Wilkinson, E.G., Crespo Garcia, I., Bygdell, J., et al. (2025). RACK1A positively

regulates opening of the apical hook in Arabidopsis thaliana via suppression of its auxin response gradient. Proceedings of the National Academy of Sciences *122*, e2407224122. https://doi.org/10.1073/pnas.2407224122.

12. Abbas, M., Alabadí, D., and Blázquez, M.A. (2013). Differential growth at the apical hook: all roads lead to auxin. Front Plant Sci *4*, 441. https://doi.org/10.3389/fpls.2013.00441.

13. Wang, Y., Peng, Y., and Guo, H. (2023). To curve for survival: Apical hook development. Journal of Integrative Plant Biology *65*, 324–342. https://doi.org/10.1111/jipb.13441.

14. Willoughby, A.C., and Strader, L.C. (2024). Apical hook opening of plant seedlings: Unfolding the role of auxin and the cell wall. Developmental Cell *59*, 3194–3196. https://doi.org/10.1016/j.devcel.2024.11.018.

15. Walia, A., Carter, R., Wightman, R., Meyerowitz, E.M., Jönsson, H., and Jones, A.M. (2024). Differential growth is an emergent property of mechanochemical feedback mechanisms in curved plant organs. Developmental Cell *59*, 3245-3258.e3. https://doi.org/10.1016/j.devcel.2024.09.021.

16. Béziat, C., and Kleine-Vehn, J. (2018). The Road to Auxin-Dependent Growth Repression and Promotion in Apical Hooks. Current Biology *28*, R519–R525. https://doi.org/10.1016/j.cub.2018.01.069.

17. Sassi, M., Ali, O., Boudon, F., Cloarec, G., Abad, U., Cellier, C., Chen, X., Gilles, B., Milani, P., Friml, J., et al. (2014). An Auxin-Mediated Shift toward Growth Isotropy Promotes Organ Formation at the Shoot Meristem in *Arabidopsis*. Current Biology *24*, 2335–2342. https://doi.org/10.1016/j.cub.2014.08.036.

18. Yeats, T.H., and Rose, J.K.C. (2013). The Formation and Function of Plant Cuticles. Plant Physiol *163*, 5–20. https://doi.org/10.1104/pp.113.222737.

19. Berhin, A., de Bellis, D., Franke, R.B., Buono, R.A., Nowack, M.K., and Nawrath, C. (2019). The Root Cap Cuticle: A Cell Wall Structure for Seedling Establishment and Lateral Root Formation. Cell *176*, 1367-1378.e8. https://doi.org/10.1016/j.cell.2019.01.005.

20. Renault, H., Alber, A., Horst, N.A., Basilio Lopes, A., Fich, E.A., Kriegshauser, L., Wiedemann, G., Ullmann, P., Herrgott, L., Erhardt, M., et al. (2017). A phenol-enriched cuticle is ancestral to lignin evolution in land plants. Nat Commun *8*, 14713. https://doi.org/10.1038/ncomms14713.

21. Ingram, G., and Nawrath, C. (2017). The roles of the cuticle in plant development: organ adhesions and beyond. J Exp Bot *68*, 5307–5321. https://doi.org/10.1093/jxb/erx313.

22. Foreman, J., Demidchik, V., Bothwell, J.H.F., Mylona, P., Miedema, H., Torres, M.A., Linstead, P., Costa, S., Brownlee, C., Jones, J.D.G., et al. (2003). Reactive oxygen species produced by NADPH oxidase regulate plant cell growth. Nature *422*, 442–446. https://doi.org/10.1038/nature01485.

23. Monshausen, G.B., Bibikova, T.N., Messerli, M.A., Shi, C., and Gilroy, S. (2007). Oscillations in extracellular pH and reactive oxygen species modulate tip growth of Arabidopsis root hairs. Proceedings of the National Academy of Sciences *104*, 20996–21001. https://doi.org/10.1073/pnas.0708586104.

24. Mangano, S., Denita-Juarez, S.P., Choi, H.-S., Marzol, E., Hwang, Y., Ranocha, P., Velasquez, S.M., Borassi, C., Barberini, M.L., Aptekmann, A.A., et al. (2017). Molecular link between auxin and ROS-mediated polar growth. Proceedings of the National Academy of Sciences *114*, 5289–5294. https://doi.org/10.1073/pnas.1701536114.

25. Kulich, I., Vladimirtsev, D., Randuch, M., Gao, S., Citterico, M., Konrad, K.R., Nagel, G., Wrzaczek, M., Cascaro, L., Vinet, P., et al. (2026). Calcium-triggered apoplastic ROS bursts balance gravity and mechanical signals for soil navigation. Science *392*, 296–300. https://doi.org/10.1126/science.adu8197.

26. Waszczak, C., Carmody, M., and Kangasjärvi, J. (2018). Reactive Oxygen Species in Plant Signaling. Annual Review of Plant Biology *69*, 209–236. https://doi.org/10.1146/annurev-arplant-042817-040322.

27. Survila, M., Davidsson, P.R., Pennanen, V., Kariola, T., Broberg, M., Sipari, N., Heino, P., and Palva, E.T. (2016). Peroxidase-Generated Apoplastic ROS Impair Cuticle Integrity and Contribute to DAMP-Elicited Defenses. Front. Plant Sci. *7*. https://doi.org/10.3389/fpls.2016.01945.

28. L'Haridon, F., Besson-Bard, A., Binda, M., Serrano, M., Abou-Mansour, E., Balet, F., Schoonbeek, H.-J., Hess, S., Mir, R., Léon, J., et al. (2011). A Permeable Cuticle Is Associated with the Release of Reactive Oxygen Species and Induction of Innate Immunity. PLoS Pathog *7*, e1002148. https://doi.org/10.1371/journal.ppat.1002148.

29. Rubinstein, B. (1971). The Role of Various Regions of the Bean Hypocotyl on Red Light-induced Hook Opening. Plant Physiol. *48*, 183–186. https://doi.org/10.1104/pp.48.2.183.

30. Silk, W.K., and Erickson, R.O. (1978). KINEMATICS OF HYPOCOTYL CURVATURE. American J of Botany *65*, 310–319. https://doi.org/10.1002/j.1537-2197.1978.tb06072.x.

31. Wang, Y., and Guo, H. (2019). On hormonal regulation of the dynamic apical hook development. New Phytol *222*, 1230–1234. https://doi.org/10.1111/nph.15626.

32. Barbier De Reuille, P., Routier-Kierzkowska, A.-L., Kierzkowski, D., Bassel, G.W., Schüpbach, T., Tauriello, G., Bajpai, N., Strauss, S., Weber, A., Kiss, A., et al. (2015). MorphoGraphX: A platform for quantifying morphogenesis in 4D. eLife *4*, e05864. https://doi.org/10.7554/eLife.05864.

33. Strauss, S., Runions, A., Lane, B., Eschweiler, D., Bajpai, N., Trozzi, N., Routier-Kierzkowska, A.-L., Yoshida, S., Rodrigues da Silveira, S., Vijayan, A., et al. (2022). Using positional information to provide context for biological image analysis with MorphoGraphX 2.0. eLife *11*, e72601. https://doi.org/10.7554/eLife.72601.

34. Vain, T., Raggi, S., Ferro, N., Barange, D.K., Kieffer, M., Ma, Q., Doyle, S.M., Thelander, M., Pařízková, B., Novák, O., et al. (2019). Selective auxin agonists induce

specific AUX/IAA protein degradation to modulate plant development. Proc. Natl. Acad. Sci. U.S.A. *116*, 6463–6472. https://doi.org/10.1073/pnas.1809037116.

35. Tanaka, T., Tanaka, H., Machida, C., Watanabe, M., and Machida, Y. (2004). A new method for rapid visualization of defects in leaf cuticle reveals five intrinsic patterns of surface defects in *Arabidopsis*. The Plant Journal *37*, 139–146. https://doi.org/10.1046/j.1365-313X.2003.01946.x.

36. Takahashi, K., Shimada, T., Kondo, M., Tamai, A., Mori, M., Nishimura, M., and Hara-Nishimura, I. (2010). Ectopic Expression of an Esterase, Which is a Candidate for the Unidentified Plant Cutinase, Causes Cuticular Defects in Arabidopsis thaliana. Plant and Cell Physiology *51*, 123–131. https://doi.org/10.1093/pcp/pcp173.

37. Panikashvili, D., Shi, J.X., Schreiber, L., and Aharoni, A. (2009). The Arabidopsis *DCR* Encoding a Soluble BAHD Acyltransferase Is Required for Cutin Polyester Formation and Seed Hydration Properties. Plant Physiology *151*, 1773–1789. https://doi.org/10.1104/pp.109.143388.

38. Wu, L., Zhou, Z.-Y., Zhang, C.-G., Chai, J., Zhou, Q., Wang, L., Hirnerová, E., Mrvková, M., Novák, O., and Guo, G.-Q. (2015). Functional roles of three cutin biosynthetic acyltransferases in cytokinin responses and skotomorphogenesis. PLoS One *10*, e0121943. https://doi.org/10.1371/journal.pone.0121943.

39. Wang, J., Sun, N., Zhang, F., Yu, R., Chen, H., Deng, X.W., and Wei, N. (2020). SAUR17 and SAUR50 Differentially Regulate PP2C-D1 during Apical Hook Development and Cotyledon Opening in Arabidopsis. Plant Cell *32*, 3792–3811. https://doi.org/10.1105/tpc.20.00283.

40. Rabe, C., and Kutschera, U. (1999). Rapid Light-Induced Enhancement of Sucrose Catabolism in the Apical Hook of Sunflower Hypocotyls. Journal of Plant Physiology *155*, 538–542. https://doi.org/10.1016/S0176-1617(99)80051-0.

41. Lorrai, R., Francocci, F., Gully, K., Martens, H.J., De Lorenzo, G., Nawrath, C., and Ferrari, S. (2021). Impaired Cuticle Functionality and Robust Resistance to Botrytis cinerea in Arabidopsis thaliana Plants With Altered Homogalacturonan Integrity Are Dependent on the Class III Peroxidase AtPRX71. Front. Plant Sci. *12*, 696955. https://doi.org/10.3389/fpls.2021.696955.

42. Chen, J., Liao, Y., and Wang, Y. (2025). HyPer7 imaging Unveils the role of hydrogen peroxide in Arabidopsis apical hook development. Biochemical and Biophysical Research Communications *774*, 152106. https://doi.org/10.1016/j.bbrc.2025.152106.

43. Thordal-Christensen, H., Zhang, Z., Wei, Y., and Collinge, D.B. (1997). Subcellular localization of H_2O_2 in plants. H_2O_2 accumulation in papillae and hypersensitive response during the barley—powdery mildew interaction. The Plant Journal *11*, 1187–1194. https://doi.org/10.1046/j.1365-313X.1997.11061187.x.

44. Li, Y., and Trush, M.A. (1998). Diphenyleneiodonium, an NAD(P)H Oxidase Inhibitor, also Potently Inhibits Mitochondrial Reactive Oxygen Species Production. Biochemical and Biophysical Research Communications *253*, 295–299. https://doi.org/10.1006/bbrc.1998.9729.

45. Raggi, S., Ferrarini, A., Delledonne, M., Dunand, C., Ranocha, P., De Lorenzo, G., Cervone, F., and Ferrari, S. (2015). The Arabidopsis Class III Peroxidase AtPRX71 Negatively Regulates Growth under Physiological Conditions and in Response to Cell Wall Damage. Plant Physiol *169*, 2513–2525. https://doi.org/10.1104/pp.15.01464.

46. Cosgrove, D.J. (2022). Building an extensible cell wall. Plant Physiology *189*, 1246–1277. https://doi.org/10.1093/plphys/kiac184.

47. Belteton, S.A., Li, W., Yanagisawa, M., Hatam, F.A., Quinn, M.I., Szymanski, M.K., Marley, M.W., Turner, J.A., and Szymanski, D.B. (2021). Real-time conversion of tissue-scale mechanical forces into an interdigitated growth pattern. Nat. Plants *7*, 826–841. https://doi.org/10.1038/s41477-021-00931-z.

48. Bidhendi, A.J., Altartouri, B., Gosselin, F.P., and Geitmann, A. (2019). Mechanical Stress Initiates and Sustains the Morphogenesis of Wavy Leaf Epidermal Cells. Cell Reports *28*, 1237-1250.e6. https://doi.org/10.1016/j.celrep.2019.07.006.

49. Chen, S., Burda, I., Jani, P., Pendrak, B., Silberstein, M.N., and Roeder, A.H.K. (2025). Fibrous network nature of plant cell walls enables tunable mechanics for development. Nat Commun *16*, 7565. https://doi.org/10.1038/s41467-025-62844-1.

50. Coen, E., and Cosgrove, D.J. (2023). The mechanics of plant morphogenesis. Science *379*. https://doi.org/10.1126/science.ade8055.

51. Verger, S., Long, Y., Boudaoud, A., and Hamant, O. (2018). A tension-adhesion feedback loop in plant epidermis. eLife *7*, e34460. https://doi.org/10.7554/eLife.34460.

52. Hamant, O., Heisler, M.G., Jönsson, H., Krupinski, P., Uyttewaal, M., Bokov, P., Corson, F., Sahlin, P., Boudaoud, A., Meyerowitz, E.M., et al. (2008). Developmental Patterning by Mechanical Signals in *Arabidopsis*. Science *322*, 1650–1655. https://doi.org/10.1126/science.1165594.

53. Sampathkumar, A., Krupinski, P., Wightman, R., Milani, P., Berquand, A., Boudaoud, A., Hamant, O., Jönsson, H., and Meyerowitz, E.M. (2014). Subcellular and supracellular mechanical stress prescribes cytoskeleton behavior in Arabidopsis cotyledon pavement cells. eLife *3*, e01967. https://doi.org/10.7554/eLife.01967.

54. Robinson, S., and Kuhlemeier, C. (2018). Global Compression Reorients Cortical Microtubules in Arabidopsis Hypocotyl Epidermis and Promotes Growth. Current Biology *28*, 1794-1802.e2. https://doi.org/10.1016/j.cub.2018.04.028.

55. Fal, K., Korsbo, N., Alonso-Serra, J., Teles, J., Liu, M., Refahi, Y., Chabouté, M.-E., Jönsson, H., and Hamant, O. (2021). Tissue folding at the organ–meristem boundary results in nuclear compression and chromatin compaction. Proc Natl Acad Sci U S A *118*, e2017859118. https://doi.org/10.1073/pnas.2017859118.

56. Lorrai, R., Erguvan, Ö., Raggi, S., Jonsson, K., Široká, J., Tarkowská, D., Novák, O., Griffiths, J., Jones, A.M., Verger, S., et al. (2024). Cell wall integrity modulates HOOKLESS1 and PHYTOCHROME INTERACTING FACTOR4 expression controlling apical hook formation. Plant Physiol *196*, 1562–1578. https://doi.org/10.1093/plphys/kiae370.

57. Jonsson, K., Porat, A., Alimchandani, V., Haque, S., Julien, É., Jönsson, H., Meroz, Y., and Routier-Kierzkowska, A.-L. (2026). Robust Organ Shape During Growth Requires Local Morphogen Signaling and Global Curvature Feedback. Preprint at bioRxiv, https://doi.org/10.64898/2026.04.02.716206 https://doi.org/10.64898/2026.04.02.716206.

58. Žádníková, P., Wabnik, K., Abuzeineh, A., Gallemi, M., Van Der Straeten, D., Smith, R.S., Inzé, D., Friml, J., Prusinkiewicz, P., and Benková, E. (2016). A Model of Differential Growth-Guided Apical Hook Formation in Plants. Plant Cell *28*, 2464–2477. https://doi.org/10.1105/tpc.15.00569.

59. Aryal, B., Jonsson, K., Baral, A., Sancho-Andres, G., Routier-Kierzkowska, A.-L., Kierzkowski, D., and Bhalerao, R.P. (2020). Interplay between Cell Wall and Auxin Mediates the Control of Differential Cell Elongation during Apical Hook Development. Curr Biol *30*, 1733-1739.e3. https://doi.org/10.1016/j.cub.2020.02.055.

60. Jonsson, K., Lathe, R.S., Kierzkowski, D., Routier-Kierzkowska, A.-L., Hamant, O., and Bhalerao, R.P. (2021). Mechanochemical feedback mediates tissue bending required for seedling emergence. Curr Biol *31*, 1154-1164.e3. https://doi.org/10.1016/j.cub.2020.12.016.

61. Narukawa, H., Yokoyama, R., and Nishitani, K. (2016). Possible pathways linking ploidy level to cell elongation and cuticular function in hypocotyls of dark-grown Arabidopsis seedlings. Plant Signaling & Behavior *11*, e1118597. https://doi.org/10.1080/15592324.2015.1118597.

62. Moyroud, E., Airoldi, C.A., Ferria, J., Giorio, C., Steimer, S.S., Rudall, P.J., Prychid, C.J., Halliwell, S., Walker, J.F., Robinson, S., et al. (2022). Cuticle chemistry drives the development of diffraction gratings on the surface of Hibiscus trionum petals. Current Biology *32*, 5323-5334.e6. https://doi.org/10.1016/j.cub.2022.10.065.

63. Riglet, L., Gatti, S., and Moyroud, E. (2021). Sculpting the surface: Structural patterning of plant epidermis. iScience *24*, 103346. https://doi.org/10.1016/j.isci.2021.103346.

64. Domínguez, E., Heredia-Guerrero, J.A., and Heredia, A. (2011). The biophysical design of plant cuticles: an overview. New Phytologist *189*, 938–949. https://doi.org/10.1111/j.1469-8137.2010.03553.x.

65. Knoche, M., and Lang, A. (2017). Ongoing Growth Challenges Fruit Skin Integrity. Critical Reviews in Plant Sciences *36*, 190–215. https://doi.org/10.1080/07352689.2017.1369333.

66. Jiang, F., Lopez, A., Jeon, S., De Freitas, S.T., Yu, Q., Wu, Z., Labavitch, J.M., Tian, S., Powell, A.L.T., and Mitcham, E. (2019). Disassembly of the fruit cell wall by the ripening-associated polygalacturonase and expansin influences tomato cracking. Hortic Res *6*, 17. https://doi.org/10.1038/s41438-018-0105-3.

67. Reynoud, N., Geneix, N., D'Orlando, A., Petit, J., Mathurin, J., Deniset-Besseau, A., Marion, D., Rothan, C., Lahaye, M., and Bakan, B. (2023). Cuticle architecture and mechanical properties: a functional relationship delineated through correlated multimodal imaging. New Phytologist *238*, 2033–2046. https://doi.org/10.1111/nph.18862.

68. Hématy, K., Sado, P.-E., Van Tuinen, A., Rochange, S., Desnos, T., Balzergue, S., Pelletier, S., Renou, J.-P., and Höfte, H. (2007). A Receptor-like Kinase Mediates the Response of Arabidopsis Cells to the Inhibition of Cellulose Synthesis. Current Biology *17*, 922–931. https://doi.org/10.1016/j.cub.2007.05.018.

69. Engelsdorf, T., and Hamann, T. (2014). An update on receptor-like kinase involvement in the maintenance of plant cell wall integrity. Annals of Botany *114*, 1339–1347. https://doi.org/10.1093/aob/mcu043.

70. Qin, X., Chen, H., Cai, W., Chen, K., Yu, B., Li, Q., Li, S., Wang, M., Chang, J., Zhang, J., et al. (2026). Turgor reduction triggers FERONIA nanodomain assembly for osmosensing in plants. Current Biology *36*, 1776-1786.e6. https://doi.org/10.1016/j.cub.2026.02.055.

71. Denness, L., McKenna, J.F., Segonzac, C., Wormit, A., Madhou, P., Bennett, M., Mansfield, J., Zipfel, C., and Hamann, T. (2011). Cell Wall Damage-Induced Lignin Biosynthesis Is Regulated by a Reactive Oxygen Species- and Jasmonic Acid-Dependent Process in Arabidopsis. Plant Physiology *156*, 1364–1374. https://doi.org/10.1104/pp.111.175737.

72. Burda, I., Brauns, F., Shipman, A., Shapland, E., Hong, L., and Roeder, A. (2025). ROS inhibits microtubule dynamics and cell growth heterogeneity during Arabidopsis sepal morphogenesis. Preprint at Developmental Biology, https://doi.org/10.1101/2025.05.09.653143 https://doi.org/10.1101/2025.05.09.653143.

73. Gorgues, L., Smokvarska, M., Mercier, C., Igisch, C.P., Crabos, A., Dongois, A., Bayle, V., Fiche, J.-B., Nacry, P., Nollmann, M., et al. (2025). GEF14 acts as a specific activator of the plant osmotic signaling pathway by controlling ROP6 nanodomain formation. EMBO Rep *26*, 2146–2165. https://doi.org/10.1038/s44319-025-00412-w.

74. Kawade, K., Li, Y., Koga, H., Sawada, Y., Okamoto, M., Kuwahara, A., Tsukaya, H., and Hirai, M.Y. (2018). The cytochrome P450 CYP77A4 is involved in auxin-mediated patterning of the Arabidopsis thaliana embryo. Development *145*, dev168369. https://doi.org/10.1242/dev.168369.

75. Lü, S., Song, T., Kosma, D.K., Parsons, E.P., Rowland, O., and Jenks, M.A. (2009). Arabidopsis *CER8* encodes LONG-CHAIN ACYL-COA SYNTHETASE 1 (LACS1) that has overlapping functions with LACS2 in plant wax and cutin synthesis. The Plant Journal *59*, 553–564. https://doi.org/10.1111/j.1365-313X.2009.03892.x.

76. Le Hir, R., Sorin, C., Chakraborti, D., Moritz, T., Schaller, H., Tellier, F., Robert, S., Morin, H., Bako, L., and Bellini, C. (2013). ABCG 9, ABCG 11 and ABCG 14 ABC transporters are required for vascular development in A rabidopsis. The Plant Journal *76*, 811–824. https://doi.org/10.1111/tpj.12334.

77. Kleinboelting, N., Huep, G., Kloetgen, A., Viehoever, P., and Weisshaar, B. (2012). GABI-Kat SimpleSearch: new features of the Arabidopsis thaliana T-DNA mutant database. Nucleic Acids Research *40*, D1211–D1215. https://doi.org/10.1093/nar/gkr1047.

78. Cutler, S.R., Ehrhardt, D.W., Griffitts, J.S., and Somerville, C.R. (2000). Random GFP::cDNA fusions enable visualization of subcellular structures in cells of *Arabidopsis* at a high frequency. Proc. Natl. Acad. Sci. U.S.A. *97*, 3718–3723. https://doi.org/10.1073/pnas.97.7.3718.

79. Marc, J., Granger, C.L., Brincat, J., Fisher, D.D., Kao, T., McCubbin, A.G., and Cyr, R.J. (1998). A *GFP–MAP4* Reporter Gene for Visualizing Cortical Microtubule Rearrangements in Living Epidermal Cells. Plant Cell *10*, 1927–1939. https://doi.org/10.1105/tpc.10.11.1927.

80. Graumann, K., Runions, J., and Evans, D.E. (2010). Characterization of SUN-domain proteins at the higher plant nuclear envelope. The Plant Journal *61*, 134–144. https://doi.org/10.1111/j.1365-313X.2009.04038.x.

81. Mouille, G., Ralet, M., Cavelier, C., Eland, C., Effroy, D., Hématy, K., McCartney, L., Truong, H.N., Gaudon, V., Thibault, J., et al. (2007). Homogalacturonan synthesis in *Arabidopsis thaliana* requires a Golgi-localized protein with a putative methyltransferase domain. The Plant Journal *50*, 605–614. https://doi.org/10.1111/j.1365-313X.2007.03086.x.

82. Mølhøj, M., Verma, R., and Reiter, W.-D. (2004). The Biosynthesis of D -Galacturonate in Plants. Functional Cloning and Characterization of a Membrane-Anchored UDP- D -Glucuronate 4-Epimerase from Arabidopsis. Plant Physiology *135*, 1221–1230. https://doi.org/10.1104/pp.104.043745.

83. Torres, M.A., Dangl, J.L., and Jones, J.D.G. (2002). *Arabidopsis* gp91^{phox} homologues *AtrbohD* and *AtrbohF* are required for accumulation of reactive oxygen intermediates in the plant defense response. Proc. Natl. Acad. Sci. U.S.A. *99*, 517–522. https://doi.org/10.1073/pnas.012452499.

84. Bonin, C.P., Potter, I., Vanzin, G.F., and Reiter, W.D. (1997). The MUR1 gene of Arabidopsis thaliana encodes an isoform of GDP-D-mannose-4,6-dehydratase, catalyzing the first step in the de novo synthesis of GDP-L-fucose. Proc Natl Acad Sci U S A *94*, 2085–2090. https://doi.org/10.1073/pnas.94.5.2085.

85. Alonso, J.M., Stepanova, A.N., Leisse, T.J., Kim, C.J., Chen, H., Shinn, P., Stevenson, D.K., Zimmerman, J., Barajas, P., Cheuk, R., et al. (2003). Genome-Wide Insertional Mutagenesis of *Arabidopsis thaliana*. Science *301*, 653–657. https://doi.org/10.1126/science.1086391.

86. Edwards, K., Johnstone, C., and Thompson, C. (1991). A simple and rapid method for the preparation of plant genomic DNA for PCR analysis. Nucl Acids Res *19*, 1349–1349. https://doi.org/10.1093/nar/19.6.1349.

87. Lampropoulos, A., Sutikovic, Z., Wenzl, C., Maegele, I., Lohmann, J.U., and Forner, J. (2013). GreenGate - A Novel, Versatile, and Efficient Cloning System for Plant Transgenesis. PLoS ONE *8*, e83043. https://doi.org/10.1371/journal.pone.0083043.

88. Clough, S.J., and Bent, A.F. (1998). **Floral dip: a simplified method for *Agrobacterium* -mediated transformation of *Arabidopsis thaliana*** . The Plant Journal *16*, 735–743. https://doi.org/10.1046/j.1365-313x.1998.00343.x.

89. Daudi, A., and O'Brien, J.A. (2012). Detection of Hydrogen Peroxide by DAB Staining in Arabidopsis Leaves. Bio Protoc *2*, e263.

90. Erguvan, Ö., Louveaux, M., Hamant, O., and Verger, S. (2019). ImageJ SurfCut: a user-friendly pipeline for high-throughput extraction of cell contours from 3D image stacks. BMC Biol *17*, 38. https://doi.org/10.1186/s12915-019-0657-1.

91. Legland, D., Arganda-Carreras, I., and Andrey, P. (2016). MorphoLibJ: integrated library and plugins for mathematical morphology with ImageJ. Bioinformatics *32*, 3532–3534. https://doi.org/10.1093/bioinformatics/btw413.

92. Schindelin, J., Arganda-Carreras, I., Frise, E., Kaynig, V., Longair, M., Pietzsch, T., Preibisch, S., Rueden, C., Saalfeld, S., Schmid, B., et al. (2012). Fiji: an open-source platform for biological-image analysis. Nat Methods *9*, 676–682. https://doi.org/10.1038/nmeth.2019.

93. Boudaoud, A., Burian, A., Borowska-Wykręt, D., Uyttewaal, M., Wrzalik, R., Kwiatkowska, D., and Hamant, O. (2014). FibrilTool, an ImageJ plug-in to quantify fibrillar structures in raw microscopy images. Nat Protoc *9*, 457–463. https://doi.org/10.1038/nprot.2014.024.

94. Demes, E., and Verger, S. (2023). High-throughput characterization of cortical microtubule arrays response to anisotropic tensile stress. BMC Biol *21*, 154. https://doi.org/10.1186/s12915-023-01654-7.

95. Barberon, M., Vermeer, J.E.M., De Bellis, D., Wang, P., Naseer, S., Andersen, T.G., Humbel, B.M., Nawrath, C., Takano, J., Salt, D.E., et al. (2016). Adaptation of Root Function by Nutrient-Induced Plasticity of Endodermal Differentiation. Cell *164*, 447–459. https://doi.org/10.1016/j.cell.2015.12.021.

Acknowledgements
We acknowledge the Knut and Alice Wallenberg Foundation for essential financing of Umeå Plant Science Centre (UPSC) via Wallenberg Initiatives in Forest Research (WIFORCE). We acknowledge the UPSC Microscopy Facility for access to imaging equipment and the Umeå Centre for Electron Microscopy (UCEM) for assistance with TEM imaging. We thank the UPSC Bioinformatics Facility (https://bioinfomatics.upsc.se) for technical support with regards to computational resources used for the FEM and whole genome sequencing data and acknowledge support to this facility from the Science for Life Laboratory, the Knut and Alice Wallenberg Foundation, the National Genomics Infrastructure funded by the Swedish Research Council, and Uppsala Multidisciplinary Center for Advanced Computational Science for assistance with massively parallel sequencing and access to the UPPMAX computational infrastructure. We thank Olivier Ali for feedback on the modeling strategy. We acknowledge Thomas Vain for the initial observation of the defect in hook maintenance of *hbk2* and *4* (Thomas Vain, PhD thesis, Swedish University of Agricultural Sciences, 2016 ISBN: 978-91-576-8711-1) and performing backcrossing and leaf sampling for these mutants. This work was financially supported by the Kempe Foundation (S.Ra.; INUPRAG to F.J.; JCK-2130 to A.H.; JCK-1732 to S.L.; JCK-1912.2 to A.A.), the Swedish Research Council (VR 2020-03420; VR 2024-04028; VR 2013-4632 to F.J., S.Ro., H.R.; VR 2020-03974 to A.A.), Stiftelsen Olle Engkvist Byggmästare (185 595 to S.Ra.), the Knut and Alice Wallenberg Foundation (S.L.; FATE, 2022.0029 to S.Ra., L.L.D.), VINNOVA (Verket för Innovationssystem) (S.L., S.Ra., H.R., S.Ro.), the European Research Council (ERC-2024-SyG STARMORPH 101166880 to S.M.D., S.Ro., J.K.-V.), Ministerio de Ciencia Innovación y Universidades of Spain (PID2024-155159NB-I00, CNS2023-143915 to K.W.), and Severo Ochoa (SO) Program for Centers of Excellence in R&D from the Agencia Estatal de Investigación of Spain [grant CEX2020-000999-S (2022 to 2025) to the CBGP to K.W.], and the Deutsche Forschungsgemeinschaft (DFG) (499026372 to J.K.-V. and CIBSS – EXC-2189; 390939984 to J.K.-V.).

Author contributions
S.Ra., H.R. and S.Ro. designed the research. S.Ra., H.R., L.L.D., Ö.E., S.M.D and F.J. performed the experiments under the guidance of S.Ro., S.V. and J.K.V. A.A. and S.L. performed preliminary data acquisition under the guidance of S.V. and S.Ro. A.H. performed the computer simulations assisted by H.R. under the guidance of M.P., K.W. and S.Ro. All authors analyzed the data. S.Ra., H.R. and S.Ro. wrote the article. All authors edited the final manuscript.

Declaration of interests
The authors declare no competing interests.

Additional information
Extended data for this paper is available online.

Supplemental information: The online version contains supplemental material.

Correspondence and requests for materials should be addressed to Stéphanie Robert.

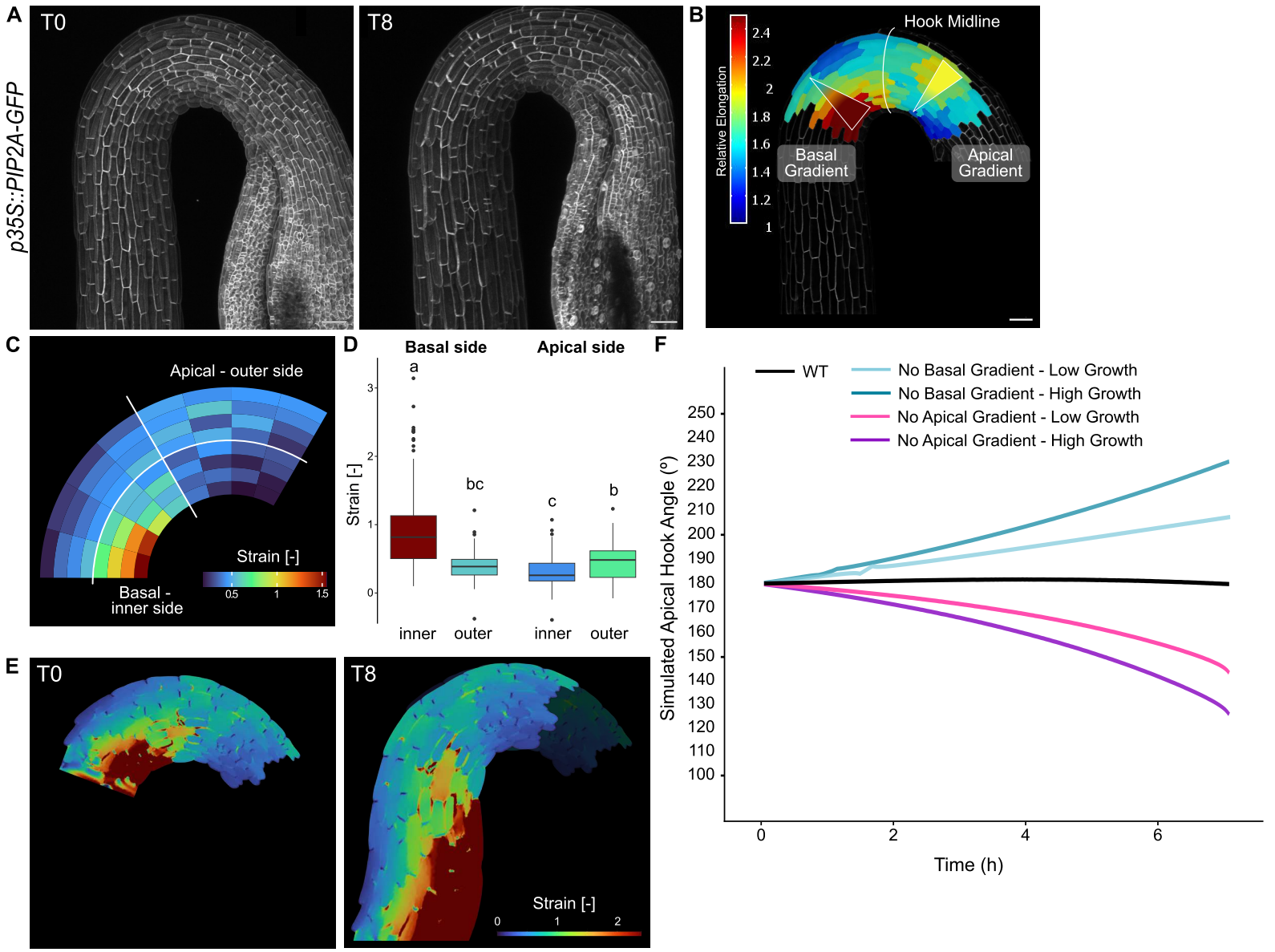


Figure 1. Characterization of differential growth patterns underlying apical hook maintenance in Arabidopsis. (A) Representative live confocal micrographs of dark-grown apical hooks of Arabidopsis expressing *p35S::PIP2A-GFP* at approximately 24–32 hours after germination (T0) and 8 hours later (T8). Scale bars represent 50 µm. (B) Schematic representation of apical hook cell elongation domains with a heatmap indicating the final:initial ratio of cell length along the principal direction of growth (PDG) over 8 hours in the seedling pictured in (A). The apical–basal and inner–outer axis definitions represented in the schematic were used for growth quantification. Scale bar represents 50 µm. (C) Correspondence matrix of *p35S::PIP2A-GFP* average longitudinal strain magnitudes, revealing two opposing apical and basal gradients of differential growth, with higher expansion on the basal–inner and apical–outer sides. Each tile represents a bin corresponding to a discrete relative position along the apical-basal and inner-outer axes, and depicts the mean elongation rate of *n* cells assigned to that position across multiple seedlings (see Figure S1D for exact *n* per positional bin). (D) Boxplots of longitudinal strain for each domain shown in (C). ≥15 cells per domain were measured from each of 6 seedlings to generate (C) and (D) *n* = 142, 86, 133 and 103 for basal inner, basal outer, apical inner and apical outer domains respectively. Different letters indicate statistically significant differences based on a Tukey *post hoc* test (α = 0.05). Box plots show the median (centre line), the IQR (inter-quartile range) (box: 25th to 75th percentiles) and whiskers extending to the most extreme values within 1.5 × IQR (E) Finite element model of a *p35S::PIP2A-GFP* apical hook mesh at T0 and the corresponding simulated geometry at T8, generated using aggregated growth properties. (F) Simulated apical hook angle kinematics of a representative *p35S::PIP2A-GFP* mesh subjected to different growth scenarios: average growth (control); average growth without the apical gradient, replaced by uniform low growth corresponding to the mean inner-domain elongation; average growth without the apical gradient, replaced by uniform high growth corresponding to the mean outer-domain elongation (see Fig. S1B); average growth without the basal gradient, replaced by uniform high growth corresponding to the mean inner-domain elongation; or average growth without the basal gradient and replaced by uniform low growth corresponding to the mean outer-domain elongation (see Fig. S1C).

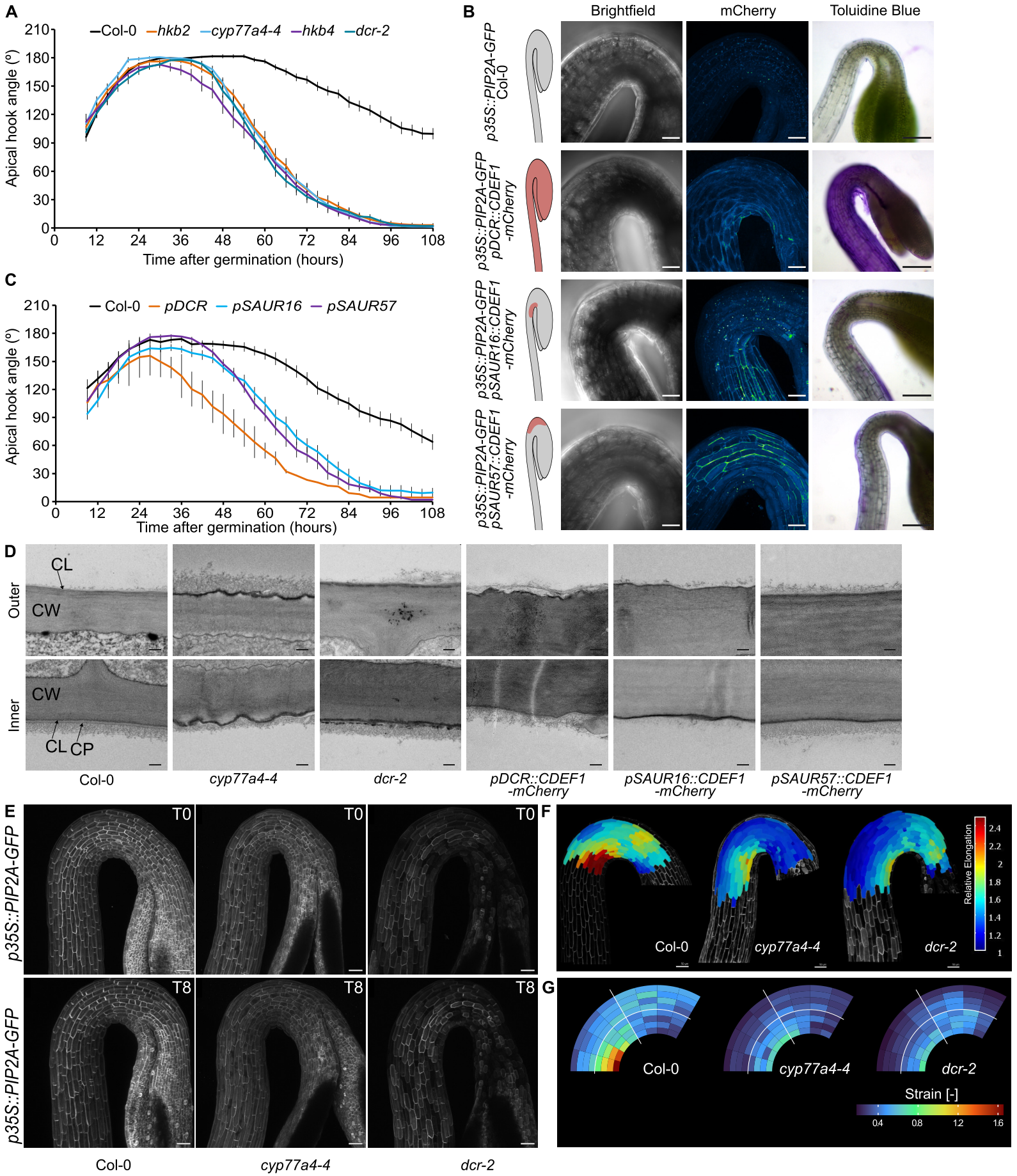


Figure 2. Cuticle integrity is essential for apical hook development. (A) Kinematics of mean apical hook angle in dark-grown Col-0 (*n*=36), *hkb2* (*n*=19), *cyp77a4-4* (*n*=23), *hkb4* (n=24) and *dcr-2* (n=23). Error bars represent standard error of the mean. (B) Schematics of mCherry expression regions (red), representative live confocal micrographs on brightfield and mCherry channels, and representative light micrographs after toluidine blue staining, of dark-grown upper hypocotyls/apical hooks of *p35S::PIP2A-GFP* in the Col-0, *pDCR::CDEF1-mCherry*, *pSAUR16::CDEF1-mCherry* and *pSAUR57::CDEF1-mCherry* backgrounds in the maintenance phase (48 hours post-germination). Scale bars represent 50 µm in the confocal micrographs and 100 µm in the light micrographs. 2–7 seedlings were imaged across ≥3 replicates. (C) Kinematics of mean apical hook angle in dark-grown seedlings of the lines shown in (B). *n* = 25, 18, 24, 20 for Col-0, *pDCR*, *pSAUR16* and *pSAUR57*. Error bars represent standard error of the mean. (D) Representative transmission electron micrographs of longitudinal sections of the inner and outer apical hook sides of the lines shown in (B) in the maintenance phase (32 hours post-germination). CW: cell wall; CL: cuticle layer; CP: cuticle proper. Scale bars represent 0.25 µm. 4–24 sections were imaged per genotype per side across 1–3 seedlings per genotype. (E) Representative live confocal micrographs of dark-grown apical hooks expressing *p35S::PIP2A-GFP* in Col-0, *cyp77a4-4* and *dcr-2* backgrounds at approximately 28 hours after germination (T0) and 8 hours later (T8). Scale bars represent 50 µm. (F) Heatmaps of final:initial cell length along PDG after 8 hours of growth overlaid on representative T0 micrographs from (E). One representative seedling per line is shown. Scale bar represents 50 µm. (G) Correspondence matrix of cell longitudinal strain in apical hooks expressing *p35S::PIP2A-GFP* in Col-0 WT, *cyp77a4-4* and *dcr-2* backgrounds. Data of time-series growth from four to six seedlings per line across three biological replicates were used to generate the matrix. See Figure S2I for exact *n* per positional bin.

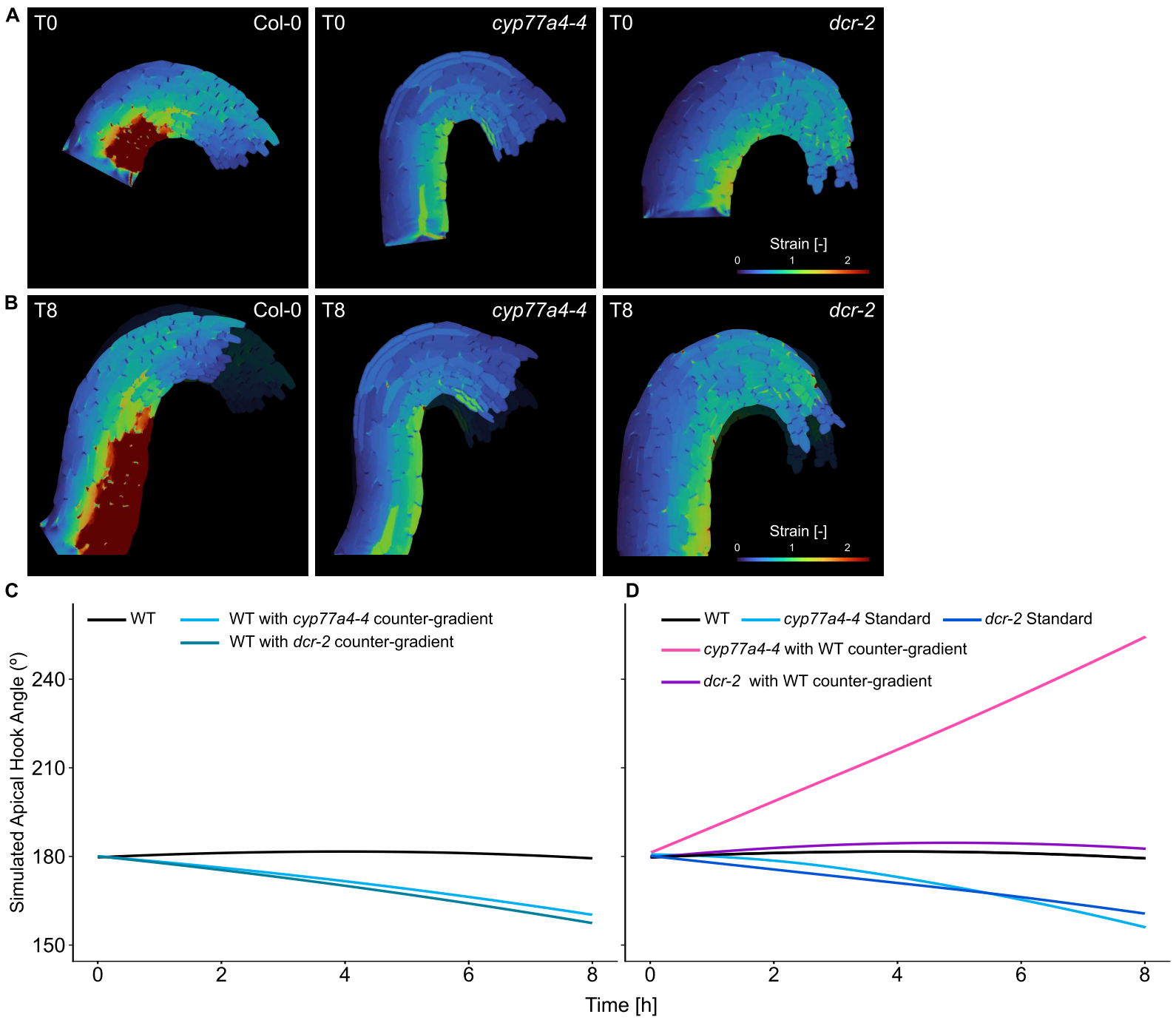


Figure 3. Altered growth properties and counter-gradients affect apical hook kinematics. (A-B) Finite element models of apical hooks of Col-0, *cyp77a4-4* and *dcr-2*, showing the initial mesh at T0 (A) and the corresponding simulated geometry after 8 hours of development (T8) (B). Simulations were generated using the average growth properties of the respective genotypes. (C) Kinematics of WT apical hook simulated using either Col-0, *cyp77a4-4*, or *dcr-2* counter-gradient profiles. (D) Kinematics of Col-0, *cyp77a4-4*, and *dcr-2* apical hooks simulated using the growth properties of their respective genotypes, as well as *cyp77a4-4* and *dcr-2* apical hook simulated with WT counter-gradient profiles.

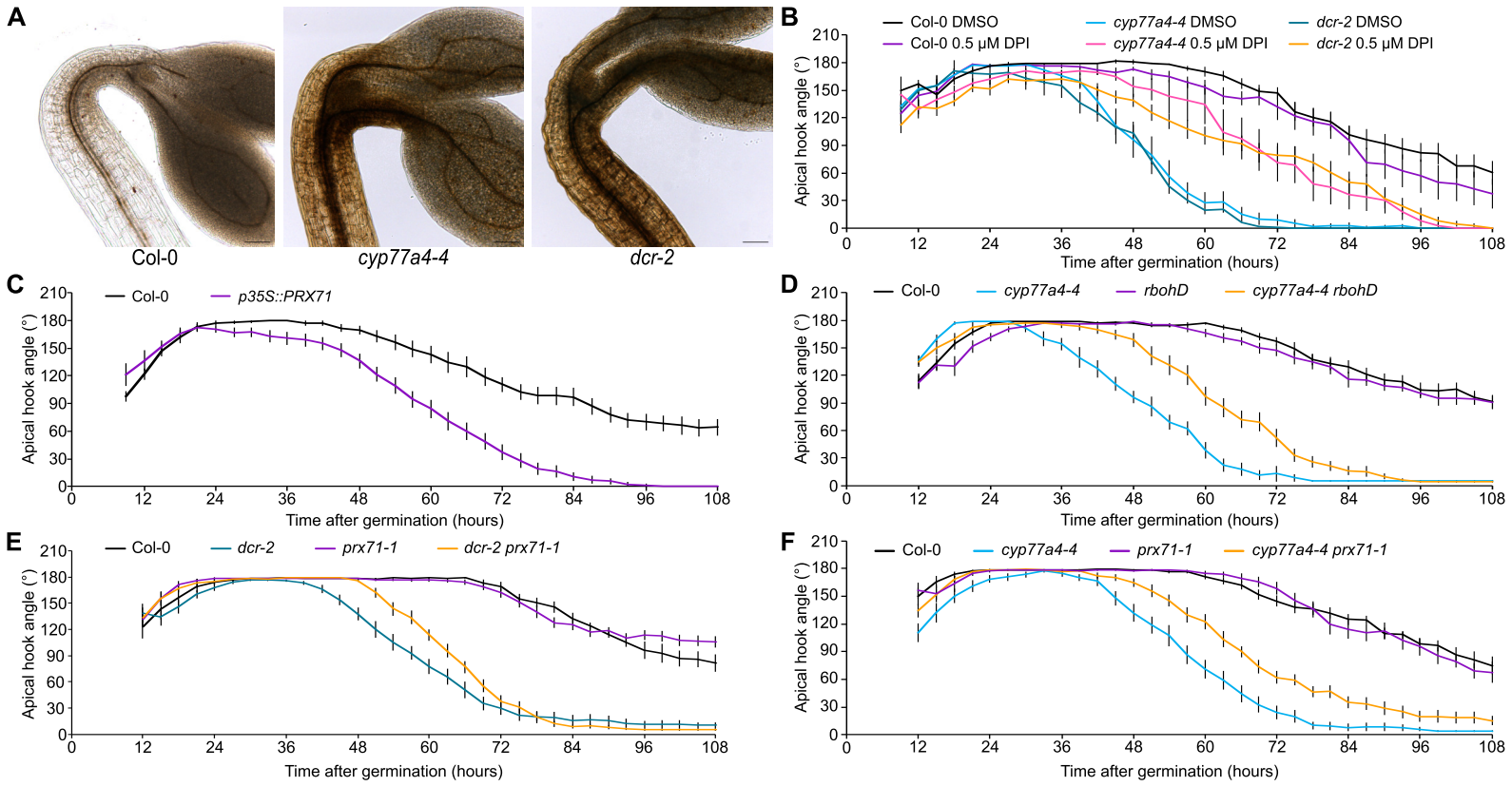


Figure 4. ROS link cuticle integrity to apical hook curvature stability. (A) Representative light micrographs of dark-grown upper hypocotyls and apical hooks of Col-0, *cyp77a4-4* and *dcr-2* in the maintenance phase (48 hours post-germination) after DAB staining. 5 to 8 seedlings were stained per each of 3 biological replicates. Scale bars represent 100 µm. (B) Kinematics of mean apical hook angle in dark-grown Col-0, *cyp77a4-4* and *dcr-2* germinated and grown on control medium (mock-supplemented with DMSO) (n = 9, 8 and 14 for Col-0, cyp77a4-4 and dcr-2) or medium supplemented with 0.5 µM DPI (n = 13, 8 and 12 for Col-0, cyp77a4-4 and dcr-2). Error bars represent standard error of the mean. (C) Kinematics of mean apical hook angle in dark-grown Col-0 (n = 12) and *p35S::PRX71* (n = 19). Error bars represent standard error of the mean. (D) Kinematics of mean apical hook angle in dark-grown Col-0 (n = 18), *cyp77a4-4* (n = 10), *rbohD* (n = 18) and *cyp77a4-4 rbohD* (n = 18). Error bars represent standard error of the mean. (E–F) Kinematics of apical hook angle in dark-grown Col-0 (n = 13 in (E), 15 in (F)), *prx71-1* (n = 14 in (E), 12 in (F)), and *dcr-2* (n = 15) and *dcr-2 prx71-1* (n = 14) (E) or *cyp77a4-4* (n = 12) and *cyp77a4-4 prx71-1* (n = 18) (F). Error bars represent standard error of the mean.

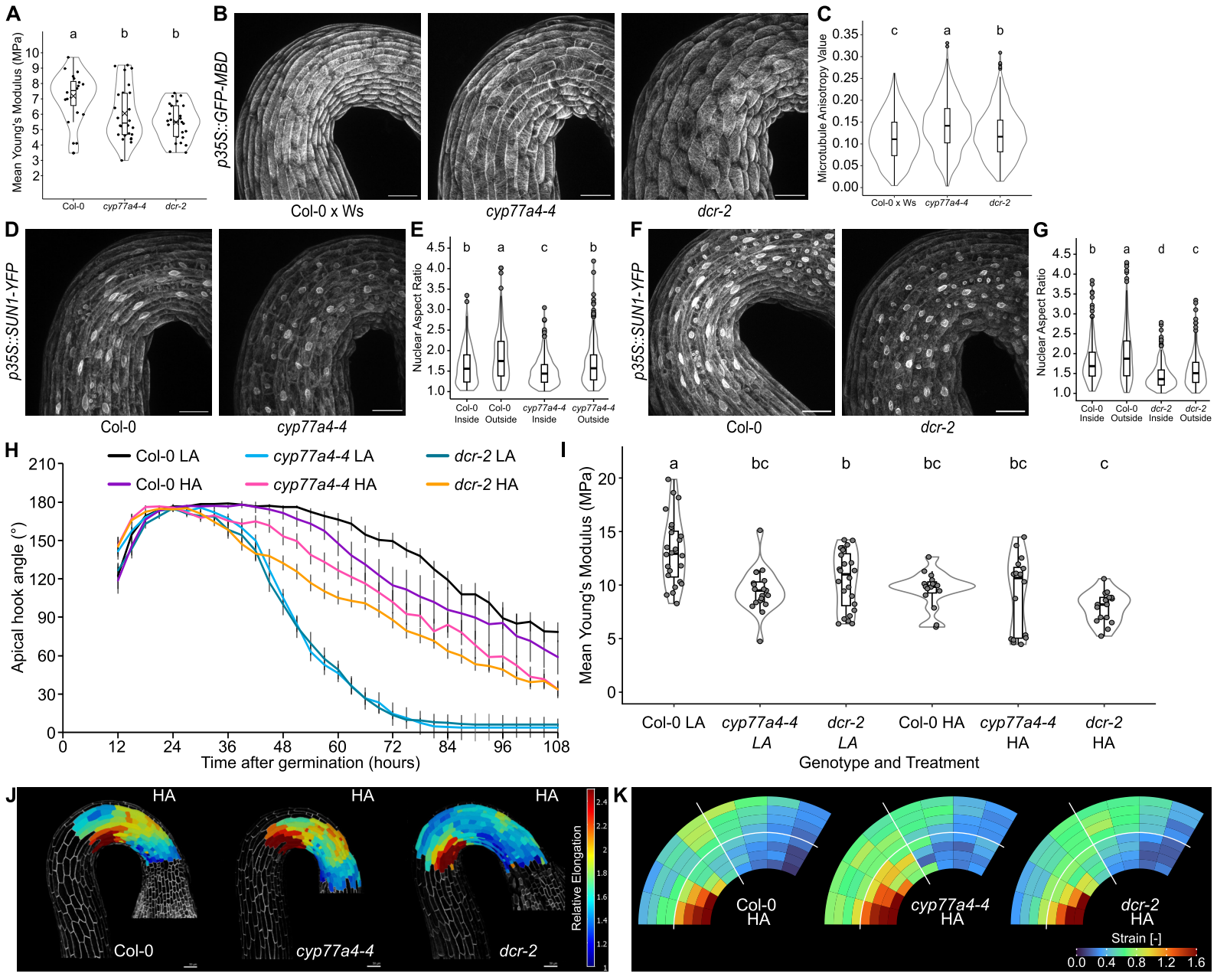


Figure 5. Mechanical cues link cuticle integrity to apical hook development. (A) Box and violin plots of Young's Modulus (cell wall indentation stiffness) of epidermal cells in basal regions of dark-grown hypocotyls expressing *p35S::PIP2A-GFP* in Col-0 (n = 20), *cyp77a4-4* (n = 26) and *dcr-2* (n = 25) backgrounds, see representative images in Fig. S4A. The average indentation stiffness measurements from ~20 positionally distinct indentations was considered as a single data point per cell, and subsequently used for statistical testing. ≥3 cells were measured for each of ≥3 seedlings per line across 3 biological replicates. Different letters indicate statistically significant differences based on one-way ANOVA and Tukey's *post-hoc* tests (α = 0.05). (B) Representative live confocal micrographs of dark-grown apical hooks of *p35S::GFP-MBD* in Col-0 x Ws-4 , *cyp77a4-4* and *dcr-2* backgrounds. Scale bars represent 50 µm. (C) Box and violin plots of microtubule anisotropy values of epidermal cells in apical hooks expressing the microtubule marker *p35S::GFP-MBD* in Col-0 x Ws-4 (n = 1042), *cyp77a4-4* (n = 828) and *dcr-2* (n = 612) backgrounds at approximately 24 hours after germination, see representative images in (B). ≥40 cells were measured for each of ≥10 seedlings per line across 3 biological replicates. Different letters indicate statistically significant differences based on Kruskal-Wallis followed by Dunn's tests (α = 0.05). (D–G) Representative live confocal micrographs of dark-grown apical hooks of *p35S::SUN1-YFP* in Col-0 and *cyp77a4-4* (D) or *dcr-2* backgrounds (F) with box and violin plots of nuclear aspect ratios (major axis length/minor axis length) of epidermal cell nuclei in the inside or outside half of apical hooks of *p35S::SUN1-YFP* in Col-0 and *cyp77a4-4* (E) or *dcr-2* backgrounds (G) at approximately 48 hours after germination, see representative images in (D) and (F). Scale bars represent 50 µm. ≥45 nuclei were measured for each of ≥9 seedlings per line across ≥3 biological replicates. Different letters indicate statistically significant differences based on Kruskal-Wallis followed by Dunn's tests (α = 0.05) (n = 244, 254, 457 and 425 for Col-0 Inside, Outside; *cyp77a4-4* Inside and Outside in (E). n = 329, 334, 385, 397 for Col-0 Inside, Outside; *dcr-2* Inside and Outside in (F)). (H) Kinematics of apical hook angle in dark-grown Col-0, *cyp77a4-4* and *dcr-2* germinated and grown on medium with low-agar (LA, 0.8% w/v agar) and high-agar (HA, 2.5% w/v agar). The means of ≥18 seedlings per line are shown; error bars represent standard error of the mean. (I) Box and violin plots of Young's Modulus (cell wall indentation stiffness) of epidermal cells in basal regions of dark-grown hypocotyls of *p35S::PIP2A-GFP* in Col-0, *cyp77a4-4* and *dcr-2* backgrounds grown on LA and HA. 5–6 cells were measured for each of 5 seedlings per line, per growth condition, with the average of 20 distinct indentations considered to be a single data point per cell. Different letters indicate statistically significant differences based on a two-way ANOVA followed by Tukey's test for honestly significant differences (α = 0.05) (On LA, n = 24, 19, 24 for Col-0, *cyp77a4-4* and *dcr-2*; on HA, n = 15, 16, 16 for Col-0, *cyp77a4-4* and *dcr-2*). (J) Heatmaps of longitudinal strain along the principal axis of growth observed in a representative seedling from T0 to T8 in apical hooks expressing *p35S::PIP2A-GFP* in Col-0, *cyp77a4-4* and *dcr-2* backgrounds grown on HA. One representative seedling per line and growth condition out of three biological replicates is shown. The heatmaps are each superimposed on the T0 micrograph of one representative seedling. Scale bar represents 50 µm. (K) Correspondence matrix of cell longitudinal strain in apical hooks expressing *p35S::PIP2A-GFP* in Col-0, *cyp77a4-4* and *dcr-2* backgrounds grown on HA. Data from four to six seedlings per line across three biological replicates were used to generate the matrix. Exact n values per bin are represented in Figure S4E. Box plots show the median (centre line), the IQR (inter-quartile range) (box: 25th to 75th percentiles) and whiskers extending to the most extreme values within 1.5 × IQR. When n is small enough, scatter plots of individual data points are included. When scatter plots are absent, individual dots represent datapoints lying outside 1.5 × IQR.

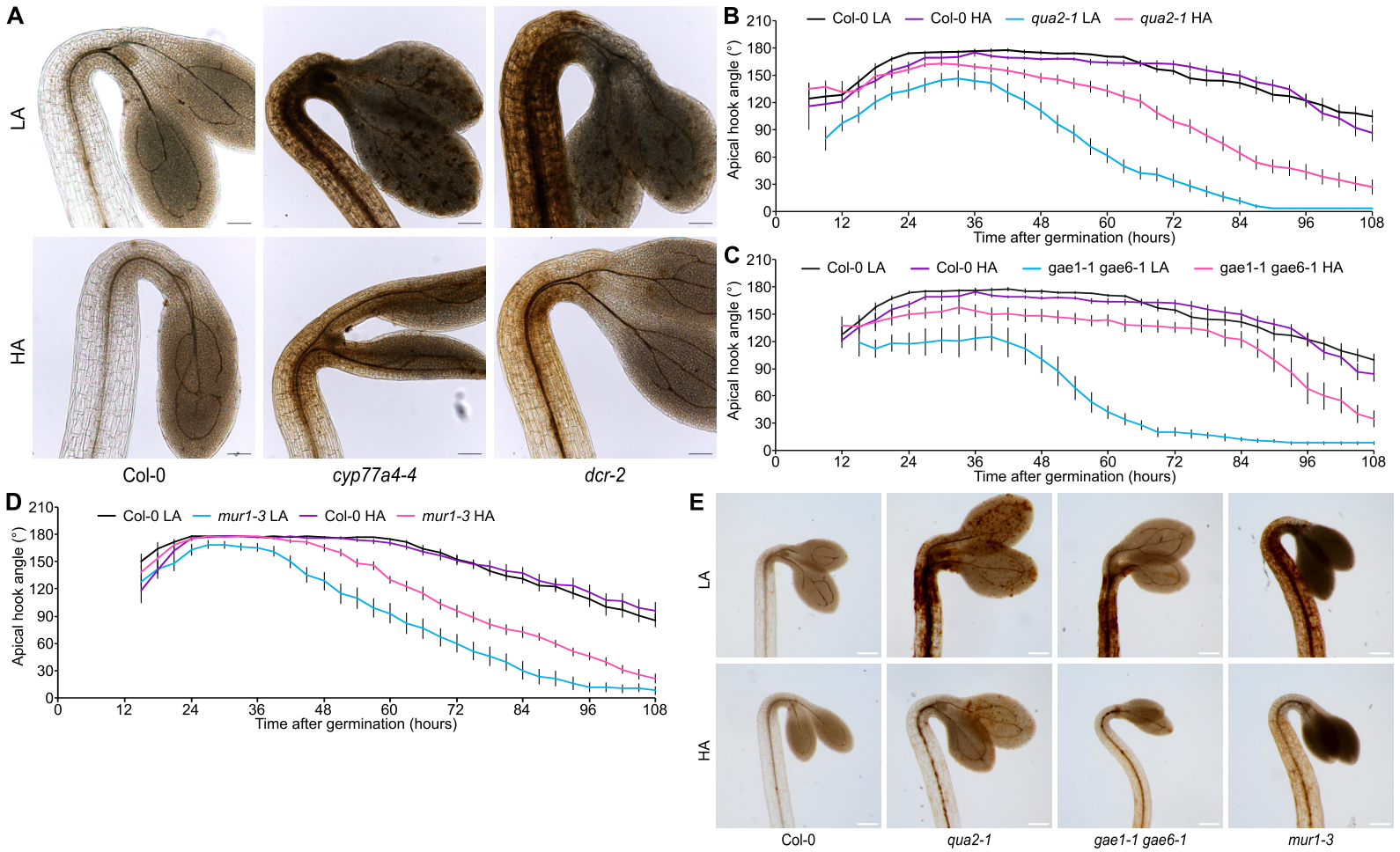


Figure 6. ROS link biomechanical cues with cuticle permeability during apical hook maintenance. (A) Representative light micrographs of dark-grown upper hypocotyls and apical hooks of Col-0, *cyp77a4-4* and *dcr-2* grown on medium with low-agar (LA, 0.8% w/v agar) and high-agar (HA, 2.5% w/v agar) in the maintenance phase (48 hours post-germination) after DAB staining. 5 to 8 seedlings were stained per each of 3 biological replicates. Scale bars represent 100 µm. (B–D) Kinematics of mean apical hook angle in dark-grown Col-0 and *qua2-1* (B), *gae1-1 gae6-1* (C) or *mur1-3* (D) germinated and grown on LA or HA. Error bars represent standard error of the mean. (E) Representative light micrographs of dark-grown upper hypocotyls and apical hooks of Col-0, *qua2-1*, *gae1-1 gae6-1* and *mur1-3* grown in the dark on LA or HA in the maintenance phase (48 hours post-germination) after DAB staining. 5 to 8 seedlings were stained per each of 3 biological replicates. Scale bars represent 200 µm. *n* values: (B) Col-0 LA = 18, HA = 18; *qua2-1* LA = 19, HA = 20. (C) Col-0 LA = 18, HA = 18; *gae1-1 gae6-1* LA = 11, HA = 10. (D) Col-0 LA = 13, HA = 15; *mur1-3* LA = 15, HA = 15.

Supplementary Files

This is a list of supplementary files associated with this preprint. Click to download.

- TableS1.pdf
- SupplementaryFigure1.pdf
- SupplementaryFigure2.pdf
- SupplementaryFigure3.pdf
- SupplementaryFigure4.pdf